

JGR Earth Surface

RESEARCH ARTICLE

10.1029/2021JF006131

Key Points:

- The inversion of seismic and long-term pore pressure data indicates the presence of free gas in cohesive shelf sediments
- Three types of free gas occurrences are distinguished based on the estimated content of bubbles and monitored overpressure patterns
- The highest gas contents are found locally at the steep shelf edge where overpressures are sufficient to initiate shear failure

Correspondence to:

S. Garziglia,
sebastien.garziglia@ifremer.fr

Citation:

Garziglia, S., Sultan, N., Thomas, Y., Ker, S., Marsset, B., Bompais, X., et al. (2021). Assessing spatio-temporal variability of free gas in surficial cohesive sediments using tidal pressure fluctuations. *Journal of Geophysical Research: Earth Surface*, 126, e2021JF006131. <https://doi.org/10.1029/2021JF006131>

Received 17 FEB 2021

Accepted 1 OCT 2021

Assessing Spatio-Temporal Variability of Free Gas in Surficial Cohesive Sediments Using Tidal Pressure Fluctuations

Sebastien Garziglia¹ , Nabil Sultan¹ , Yannick Thomas¹, Stephan Ker¹ , Bruno Marsset¹, Xavier Bompais², Patrice Woerther², Christoph Witt³ , Achim Kopf³, and Ronan Apprioual¹

¹Ifremer, Unité Géosciences Marines, Plouzané, France, ²Ifremer, Unité Recherche et Développements Technologiques, Plouzané, France, ³MARUM—Center for Marine Environmental Sciences, University of Bremen, Bremen, Germany

Abstract From a geohazard assessment perspective, the distribution, content, and dynamics of free gas in surficial sediment were addressed by imaging and monitoring the upper 15 m beneath the shelf offshore Nice, France. Based on high-resolution seismic data covering three sites where pore pressure was recorded over three and a half years, the presence of free gas was determined in the upper 2.75–14.75 m of cohesive, silty clay. Seismic velocity changes delineate two layers with gas volume fractions ranging from 0.12% to 1.89%. By considering the tidal response recorded by eight pore pressure sensors, estimates of gas volume fractions vary from 0.26% to more than 9.4% on a spatio-temporal scale which cannot be achieved with seismic data. To depict spatio-temporal patterns three types of free gas occurrence (FGO) were distinguished. Type 3 FGO uniquely showed sawtooth fluctuations in overpressure of 27%–45% of the hydrostatic effective stress as evidence of bubble growth and rise. The other two types showed long-term overpressure trends indicative of a situation whereby bubble growth has ceased. Type 1 FGOs are distinguished from type 2 by their gas volume fraction lower than 9.4% and ratios of overpressure to hydrostatic effective stress lower than 0.3. Values higher than this threshold are considered sufficient for shear failure to initiate from the steep shelf edge (>20°). Beyond site-specific insights, the distinction of FGO from their overpressure levels yields testable implications for the dynamics of methane in sediments.

Plain Language Summary Increased awareness of the role of gas bubbles in surficial sediments with regard to the stability of submarine slopes has stressed the need to quantify their distribution, content, and evolution with time. This was addressed by imaging and recording pressure fluctuations of shallow subsurface marine sediments. Both methods agreed in delineating the broad distribution of gas in these clayey deposits. However, they provided contrasting estimates of gas content which could be related to their distinct sensitivity to local changes. The analysis of the results obtained from the pressure records led to the recognition of three types of gas accumulations which cannot be discerned by imaging the subsurface. One type distinguishes from the others by showing episodic fluctuations in gas content and pressure ascribed to the growth and rise of bubbles. The other two types show trends in pressure suggesting that bubble growth has ceased. Of these two types, the one which is characterized by the highest gas content and pressure level is also considered to have the potential to initiate local shear failure in sediment. On a broader perspective, field evidences reported in this study provide constraints and testable implications for models addressing the transfer of methane to the atmosphere.

1. Introduction

Recognition of the widespread occurrence of gas in shallow marine sediments has sustained interest for its significance in offshore engineering activities, slope stability, and climate change (Egger et al., 2018; Fleischer et al., 2001; Kaminski et al., 2020; Sills & Wheeler, 1992). On continental shelves, methane is commonly produced by the biogenic degradation of buried organic matter (Fleischer et al., 2001; Mogollón et al., 2011). Due to the low solubility of methane in these shallow water settings, levels of dissolved gas can reach supersaturation and lead to the formation, growth, and rise of gas bubbles (Boudreau, 2012; Mogollón et al., 2011). Because temperature, pore pressure, and salinity influence biogenic reactions and determine

gas solubility, they in turn control the distribution and content of gas bubbles in sediment (Mogollón et al., 2011). Concerns over the environmental and engineering implications of the presence and fate of gas in sediments have motivated the use of remote sensing techniques for mapping and quantification purposes (Cevatoglu et al., 2015; Dale et al., 2009; Leighton & Robb, 2008; Morgan et al., 2012; Tóth et al., 2014; Vardy et al., 2017). Seismic reflection surveys have proved to be successful in detecting gas-bearing sediments since even small quantities of bubbles can cause a marked reduction in compressional wave velocity (V_p) and increases in both compressional wave attenuation and scattering (Gardner, 1999; Wilkens & Richardson, 1998). The reduction in compressional wave velocity has been experimentally and theoretically related to the greater compressibility, or lower bulk modulus, of sediments in the presence of undissolved gas (Anderson & Hampton, 1980; Sills et al., 1991). This provided a route for estimating free gas concentrations from seismic velocity data using rock physical models, under the assumptions that bubbles are homogeneously contained in the pore fluid (Ecker et al., 2000; Tóth et al., 2014) or patchily distributed as a “sediment replacing” phase (Ker et al., 2019). The merits of these seismic-based approaches lie in their ability to yield estimates of the spatial variability of free gas concentrations over large areas. However, limitations inherent to the spatial resolution of seismic data together with uncertainties in velocity picking often preclude analyses at scales below 1 or 2 m (Barrett et al., 2017; Tóth et al., 2014). Following a theoretical examination of the effects of free gas on pore fluid compressibility, Wang et al. (1998) pointed out that tidally induced pore pressure variations can be used as a method complementary to acoustic velocity to constrain the quantity of free gas. Along this line, Sills and Thomas (2002) concluded the analysis of field tests by noting that the pore pressure response to ocean waves and tides can be used to provide an indication of how and how much gas is present in a sediment. Yet, the potential of these findings for the evaluation of the fine-scale distribution of gas-bearing sediments has not been realized. The purpose of this study is to expand on the results of Wang et al. (1998) and Sills and Thomas (2002) by analyzing seismic data and the tidal response of pore fluid pressure down to about 15 m below the seafloor (mbsf). The central approach of this study draws on the continuous monitoring over three and a half years of differential pore pressure and temperature using three piezometers installed in shelf sediments, offshore Nice Airport. In this area, affected by a destructive submarine landslide in 1979, gas charging and its impact on sediment properties were identified as key factors to quantify to assess the possibility that slope failures may occur again (Sultan, Savoye, et al., 2010; Vanneste et al., 2014). The combination of the geophysical and geotechnical approaches developed in this study contributes to this goal by providing, for the first time, estimates of the distribution and amount of free gas in the sector of the shelf which according to Leynaud and Sultan (2010) is the most susceptible to failure.

2. Geological Setting

The study area is located near the mouth of the River Var on the narrow continental shelf which extends typically less than 1.3 km offshore Nice Airport in SE France (Figure 1). It lies in water depths of 20–30 m and is bordered to the south by a steep (as much as 30°) continental slope affected by retrogressive failures (Kelner et al., 2016; Migeon et al., 2012). As a result of the landslide which removed an estimated volume of $8.6 \times 10^6 \text{ m}^3$ of material on October 16, 1979, slopes as steep as 40° border the south-western and north-western parts of the study area (Kelner et al., 2016). The continental shelf and upper slope are covered by up to 50 m of silty clay sediments deposited at the front of the River Var delta (Anthony & Julian, 1997; Kopf et al., 2016). These Holocene deposits overlie an up to 80 m thick sequence of coarser-grained deltaic and fluvial deposits comprising abundant thin peat interbeds above the basal Pliocene conglomerate (Anthony & Julian, 1997). The fact that the sandy gravel deposits of fluvial origin constitute an artesian aquifer (Guglielmi & Prieur, 1997) was taken by Dan et al. (2007) as an indication that groundwater flow contributed to the initiation and development of the failure which occurred on October 16, 1979. Beyond this event, Stegmann et al. (2011) used long-term pore pressure measurements to estimate that the transmission of artesian pressure could be responsible for the presence of one of the shear zones that Sultan, Savoye, et al. (2010) detected on the shelf using piezocone soundings. This suspicion was recently confirmed by Sultan et al. (2020) who relied on longer-term pore pressure data recorded down to 30 mbsf. Their study revealed that lateral artesian flow through permeable layers induced overpressures up to 60 kPa at about 26 mbsf. The consequent decrease in effective stress was shown to be the major factor promoting the development of shear zones beneath the shelf. However, this did not rule out the possibility put forward by Steiner et al. (2015) that gas charging also contributes to weakening silty clay sediments. They built their

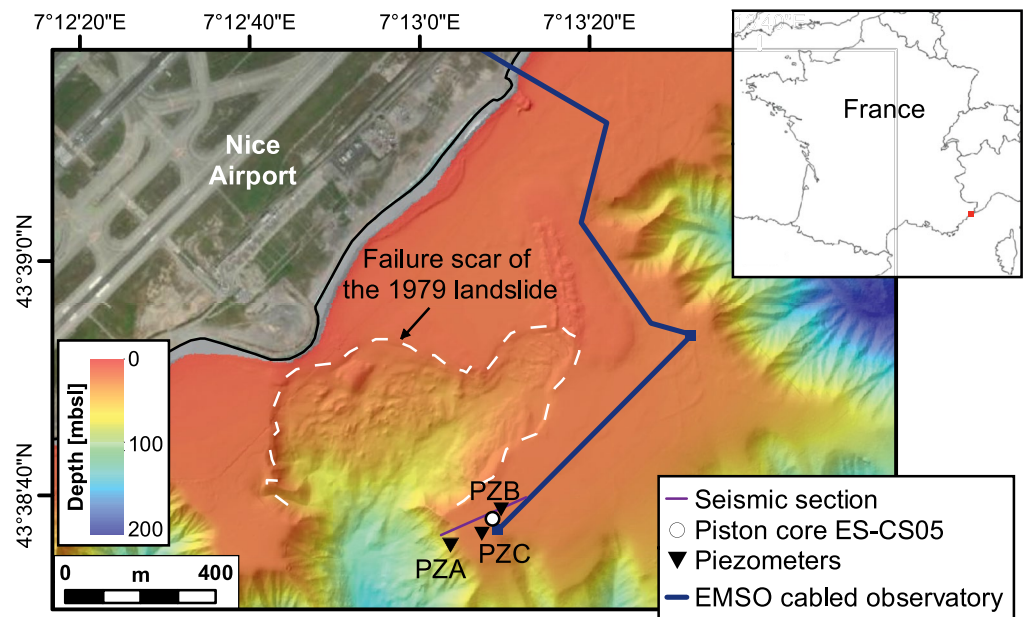


Figure 1. Location map of the study area off the Nice Airport.

arguments on reported observations of gas bubbles in sediment cores and acoustic blanking on high-resolution seismic data. Yet, in view of the lack of quantitative data regarding the amount and distribution of gas bubbles in sediment, the influence of gas charging on slope stability remains speculative.

3. Materials and Methods

3.1. Seismic Data and Interval Velocities

During a geophysical survey conducted by Ifremer in May 2015 (STEP 2015 cruise) 22 multi-channel seismic lines were acquired over the continental shelf offshore Nice Airport using a 1200 J Sparker source. The seismic data were recorded on a 48-channel streamer of 230 m long with a trace spacing of 3.125 m, which was towed at a depth of 0.6 m. One Automatic Identification System was deployed on the seismic source and two others on the head and tail of the streamer to ensure positioning with meter accuracy.

The pre-processing of the seismic data presented in this study (see location in Figure 1) included common midpoint binning, spherical divergence correction, 125–2,500 Hz bandpass filtering, normal moveout correction, and signature deconvolution. To preserve the high-frequency content of the source by avoiding too high incidence angles, only the first 24 traces were stacked (i.e., maximum offset of 80 m). This provided seismic data with a frequency range of 175–850 Hz.

Detailed Root Mean Square velocity (V_{rms}) analyses were performed on super gathers every 1 m. After the picking of velocities on semblance panels, interval velocities were computed using the Dix equation. Stack and post-stack time migration were then applied using this velocity field.

The method developed by Hajnal and Sereda (1981) was used to provide some quantification of the uncertainty in interval velocity calculation as a function of V_{rms} uncertainty and uncertainty in the arrival time of a picked velocity, T_{rms} . For this purpose, T_{rms} was set as a constant equal to the resolution of the semblance spectra, that is 0.5 ms. Following Colin et al. (2020), V_{rms} uncertainties were obtained by considering all V_{rms} within 98% of the picked semblance maximum. As a result uncertainties in interval velocity estimates ranged from 36 to 198 m/s depending on the depth and thickness of the sediment layer.

3.2. Sediment Core

The 10.5 m long sediment core ES-CS05 used in this study was recovered at 20 m water depth using a Calypso piston corer during the ESTIME cruise (2015) on the *R/V Pourquoi Pas?* It was cut into 1-m long sections, sealed and logged with a Multi Sensor Core Logger (MSCL) from Geotek to obtain bulk density and compressional wave velocity (V_p at 230 kHz) profiles. Pore-water extraction was subsequently carried out onboard at a sampling interval of 30 cm. This was achieved by drilling small holes along whole core sections to place Rhizon samplers (Ruffine et al., 2013; Seeberg-Elverfeldt et al., 2005) connected to 10 ml syringes for water collection. Pore-water samples and sediment sections were then stored at 4°C before laboratory analysis.

3.2.1. Pore-Water Analyses

Chloride and sulfate concentrations in pore-water samples were measured by ion chromatography on an 861 Advanced Compact Ion Chromatograph from Metrohm. After calibration with the standard seawater from the International Association for Physical Sciences, the accuracy of the measured concentrations is estimated to be in the order of $\pm 3\%$.

The concentrations of dissolved organic carbon (DOC) in pore-water were determined with the nonpurgeable organic carbon (NPOC) method on a Shimadzu TOC-L CSH. To remove inorganic carbon, samples were acidified with HCl and purged with compressed air before analysis by high-temperature, catalytic oxidation-nondispersive spectroscopy.

3.2.2. Bulk-Sediment Analyses

The bulk density and V_p profiles obtained with the MSCL were used to select and preserve eight samples for oedometer tests. According to ASTM D2435/D2435M-11 (ASTM, 2011) these fine-grained samples were placed in 50 mm diameter oedometer cells and incrementally loaded up to 1,765 kPa to determine their recompression index (Cr) and compression index (Cc). They were subsequently incrementally unloaded to determine their swelling index (Cs).

The remaining parts of the whole core sections were split into two halves, one for visual analysis and the other for acoustic measurement and sub-sampling. Acoustic measurements were carried out by pushing an ultrasonic fork into the sediment at a spacing of 10 cm. Two transducers in the fork served to produce a 1-MHz compressional wave from one branch and to record its travel time to the opposite branch located 7 cm apart. This approach aimed at ensuring a better acoustic coupling between the transducers faces and the sediment than with the ultrasonic system of the MSCL which may suffer limitations if the core liner is not full.

Every 10–30 cm, about 30 g of bulk sediment were sampled to determine its mineralogical composition, total organic carbon (TOC) concentration, and water content. Following the sample preparation method described by Chéron et al. (2016), X-Ray powder diffraction was carried out using a D8 Advance Bruker diffractometer to obtain quantitative estimates of the mineralogical composition of the sediment. As for pore-water samples, the TOC of the sediment was determined with the NPOC method on a Shimadzu TOC-L CSH. The water content of the sediment was measured as weight loss after 24 h in an oven at 105°C.

3.3. Pore Pressure and Temperature Data

Two types of piezometers developed in Ifremer were used to monitor pore pressure and temperature at different levels below the seafloor. The first one, here referred to as the “V2-type,” has been described and used by Stegmann et al. (2011) as “PZ2 piezometer.” It is a modular instrument containing up to 10 sensor modules and a data logger accessible at the seabed (Figure 2). Modules containing differential pressure and temperature sensors can be mounted on the 6 cm diameter shaft with a minimum spacing of 75 cm. Temperature is measured inside the shaft with an accuracy of $\pm 0.05^\circ\text{C}$ in the 0–50°C working range. The Hastelloy differential pressure transducers from Keller have a maximum working range of 200 kPa and a rated accuracy of ± 0.5 kPa. Pore pressure is sensed through a sintered porous metal disc while the ambient pressure of the water column is sensed through the seawater-filled interior of the shaft (Figure 2). To ensure that this provides a direct basis for evaluating excess pore pressures the full saturation of the measuring

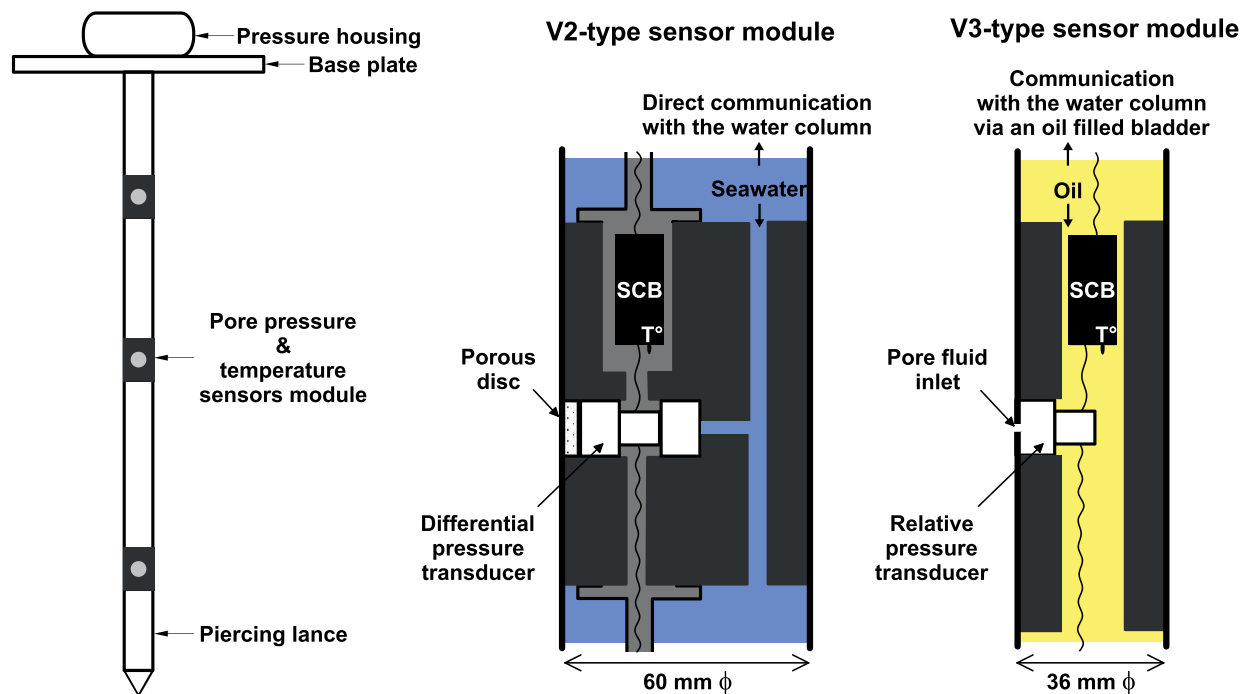


Figure 2. Left: Schematic diagram of piezometers. Right: Illustration of the different sensor modules on piezometers of V2 and V3 types. Note the location of the temperature sensor (T°) on the signal conditioning board (SCB).

system is achieved by leaving piezometers suspended vertically in the seawater for at least 15 min. By allowing stabilization of both the pressure and temperature sensors in hydrostatic and stable thermal conditions, this procedure also aims at checking piezometer readings and correcting them for possible drifts. The driving force necessary for the installation of piezometers is provided by a weight stand which can be acoustically released and recovered once the base plate rests at the seabed. In the study area, this way of installation has placed limitations on penetration such that the monitoring by the two V2-type piezometers presented in this study was restricted to the upper 5.55 m (PZ2B) and 7.05 m (PZ2A) of shelf sediments (see characteristics in Table 1).

To overcome penetration limitations, a prototype, here referred to as the V3-type piezometer, has been developed to be inserted into the sediment with the Penfeld seabed rig (Meunier et al., 2004). Similarly to the rod that the Penfeld usually uses for soundings with 10 cm² piezocones, the 3.6 cm diameter shaft of the V3-type piezometer was coiled onto a drum, straightened by plastic deformation, and pushed down to 30 m below the seafloor at a rate of 2 cm/s. It was equipped with 20 sensor modules spaced 1–2 m apart with the first one 25 cm above the seafloor (Table 1). Since these modules and the measuring system had to fit into a small diameter shaft, they differ from those of V2-type piezometers. The main difference is related to the use of relative pressure sensors to measure, through 0.4 cm diameter inlets, the difference between the sediment pore pressure and the oil-filled shaft which transmits the ambient pressure of the water column via a bladder (Figure 2). Because sensors with working ranges of 200 and 500 kPa were used, the pore pressure data presented in this study were measured by piezometer PZC with a rated accuracy of ± 0.5 kPa in the

Table 1
Characteristics of the Piezometers Used in This Study

Name in this study	Original name	Type	Coordinates	Water depth (m)	Length (m)	Number of sensors	Recording period
PZ2A	ST4-PZ2L-01B	V2	N43.6433 E7.2178	31	7.05	6	28/01/2014 08/05/2019
PZ2B	ST5-PZ2L-01	V2	N43.6442 E7.2192	20	5.55	6	30/04/2015 20/08/2019
PZC	SPF-PZ3L-01	V3	N43.6435 E7.2186	21	28.38	20	15/10/2015 21/06/2019

upper 7 m below the seafloor and ± 1.25 kPa deeper. On both types of piezometers, temperature was measured with an accuracy of $\pm 0.05^\circ\text{C}$. The data logger was similar to that of V2-type piezometers. However, the data logger could not have been connected before and during the deployment of the V3-type piezometer but later with diver assistance. This implies that the pressure and temperature data from this piezometer PZC could not have been corrected for possible drifts in pressure and temperature after their calibration in the laboratory. For this reason, the physically unrealistic negative values of pressure recorded by sensors located at 6.75 m (P6) and 11.75 m (P10) are discarded from this study. Additionally, although 20 sensor modules were mounted on this piezometer only those located in the upper 14.75 m of sediment are considered hereafter as this corresponds to the penetration depth of the seismic data.

As shown in Figure 1, the three piezometers here mentioned were deployed in a relatively restricted area of the shelf with the first purpose of monitoring active processes where Leynaud and Sultan (2010) revealed a 50% probability of slope failure. The V2-type piezometer PZ2A was the first to be installed during the STEP 2014 cruise (Table 1), close to the shelf edge, at the site where Sultan, Savoye, et al. (2010) identified gas bubbles in a sediment core (KGMO-06). The identification of gas-free and gas-bearing intervals on this core influenced the location of the six sensor modules along the 7.05 m long lance of PZ2A. During the STEP 2015 cruise (Table 1), the other V2-type piezometer PZ2B was installed away from the shelf edge where no evidence of the presence of free gas in sediment was previously reported. To avoid operational difficulties encountered during the previous installation of PZ2A, the lance of PZ2B was only 5.55 m long. This smaller lance was however equipped with the maximum possible number of sensor modules. The V3-type piezometer PZC was installed later in 2015 during the ESS-PENF50 cruise (Table 1) with the first aim of reaching a shear zone that Sultan, Savoye, et al. (2010) identified between 18 and 30 mbsf. The PZC data recorded in this depth interval were used by Sultan et al. (2020) to study the shear zone and underlying processes. For conciseness and clarity, they are not considered in this study which focuses on the upper 15 m of sediments.

All piezometers were deployed as stand-alone instruments each with an integrated data logger and power supply stored in a pressure housing (Figure 2). However, from September 2016, piezometers PZ2A and PZC have been connected to a specially developed subsea cabled observatory ensuring both the power supply of the instruments and the transmission of their measurements in real time. As detailed in Bompais et al. (2019), the infrastructure includes two subsea stations connected to a shore station by an electro-optical cable allowing remote access through the internet and automatic data transmission to data centers. In 2016, this infrastructure became one of the research facilities of the European Multidisciplinary Seafloor and water column Observatory-European Research Infrastructure Consortium (EMSO-ERIC). Since then, the EMSO-LIGURE Nice infrastructure has not suffered any failure in providing real-time data at a sampling rate of 2 min (Garziglia et al., 2018a, 2018b). However, as indicated in Table 1, piezometers PZ2A and PZC respectively stopped working in May and June 2019, for reasons which remain unknown. No similar issue occurred to piezometer PZ2B which fully autonomously recorded data at a sampling rate of 3 min from its deployment in 2015 until the recovery of its data logger by divers in August 2019. All piezometer data have been subsampled at 10-min intervals to coincide with the tide gauge data presented hereafter.

3.4. Sea Level Height Data

The tide gauge located in the port of Nice, 5 km east of the study area provided sea level height values (<http://dx.doi.org/10.17183/REFMAR>). These values were recorded at 10-min intervals with a radar sensor (BM70 A from Krohne) operated by the French Hydrographic and Oceanographic Service of the Navy (SHOM), as part of the coastal network Réseau d'Observation du Niveau de la Mer (RONIM) (Martín Míguez et al., 2008). This implies that the time series has been quality-checked to comply with the requirements of French standards (SHOM, 2005) including a timing accuracy better than 10 s, a level accuracy better than 1 cm, and reference to a chart datum defined as the level of the lowest astronomical tide. Values of sea level were used to compute tidal pressure fluctuations using a density of 1.028 g/cm^3 for seawater.

3.5. Effective Medium Model for Estimating Free Gas Content From Seismic Velocities

The estimation of free gas content from interval seismic velocities relied on the three-phase effective medium model proposed by Helgerud et al. (1999). It is based on the model developed by Dvorkin et al. (1999)

to relate the bulk (K) and shear (G) moduli of the dry sediment frame to porosity, mineralogy, and effective stress. Following the approach adopted by Sultan et al. (2007), the stiffness of the dry frame is related to porosity and effective stress using values of compression index (C_c) and void ratio at 0.01 kPa (e_0) obtained from oedometer tests. These values also serve to determine the bulk density of fully saturated sediments. Together with the bulk and shear moduli calculated at full water saturation using Gassmann's equations, bulk densities are used to derive water-saturated compressional wave velocities ($V_{p_{sat}}$). Finally, the gas volume fraction in the sediment, n_g , (the proportion of gas volume to total sediment volume) is estimated from the difference between $V_{p_{sat}}$ and seismic velocities ($V_{p_{seis}}$). As proposed by Helgerud et al. (1999), two end-member estimates are obtained with the fluid substitution procedure by considering that (a) gas is homogeneously distributed in the pore space or that (b) gas occurs in patches larger than the average pore size and is fully surrounded by water-saturated sediment. In both cases, the density (ρ_g) and adiabatic bulk modulus (K_g) of the gaseous phase were considered to evolve with temperature (T) and hydrostatic pressure (P) using the approximations recommended by Mavko et al. (2009) after Batzle and Wang (1992).

3.6. Geotechnical Model for Estimating Free Gas Content From Pore Pressure Measurements

Sediment pore pressures were measured relative to the current hydrostatic pressure using both V2 and V3 type piezometers (Figure 2). Accordingly, in the presence of free gas in sediment, a change in height of the water column is anticipated to affect the measured differential pore pressure because of the high compressibility of gas bubbles compared to seawater. Over the past few decades, several authors (i.e., Mei & Foda, 1981; Sobkowicz & Morgenstern, 1984; Tørum, 2007; Wang et al., 1998) have built on Biot's theory of poro-elasticity to consider the impact of wave or tidal loading on the pressure and compressibility of pore fluids. The present work relies on the closed-form solution presented and validated against experimental data by Sobkowicz and Morgenstern (1984). It consists of a simple quadratic equation (Equation 1) relating the change in pore pressure (Δu) to the change in total stress ($\Delta\sigma$):

$$A.\Delta u^2 + B.\Delta u + C = 0 \quad (1)$$

where A , B , and C are function of the sediment porosity (n), the degree of water saturation (S_r), the absolute pressure (P_0), the change in total stress ($\Delta\sigma$), Henry's law constants for gas solubility in water (H) and sediment and water compressibilities (β_T and β_L) according to Equations 2–4:

$$A = \beta_T + n.S_r.\beta_L \quad (2)$$

$$B = \beta_T(P_0 - \Delta\sigma) + n(\beta_L.S_r.P_0 + 1 - S_r + S_r.H) \quad (3)$$

$$C = -\beta_T.\Delta\sigma.P_0 \quad (4)$$

The compressibility of seawater β_L was considered as a constant equal to $4.28 \times 10^{-7} \text{ kPa}^{-1}$ (Fredlund, 1976) while the swelling indices, C_s , obtained from oedometer tests were used to define sediment compressibility β_T . The change in pore pressure also depends on the liquid/gas saturation pressure ($u_{l/g}$) below which gas exsolution begins. It is important to note that in the Sobkowicz and Morgenstern (1984) model, the gas is considered as an ideal gas so its bulk modulus equals the absolute pressure, P_0 .

Measured changes in differential pore pressure (Δu) and tidal pressure ($\Delta\sigma$) were used to estimate degrees of water saturation, S_r , by solving Equation 1. This implied the application of the least-squares method with error minimization between measured and predicted Δu values. Gas volume fractions, n_g , were obtained from the porosity (n) and degree of water saturation using $n_g = n(1 - S_r)$.

4. Results

4.1. Seismic Reflection and Velocity Data

The 230 m-long seismic section ST5-014 crosses the western border of the Nice continental shelf where three piezometers were installed and sediment core ES-CS05 was recovered (Figures 1 and 3). It basically shows two distinct facies before the arrival of the first seabed multiple. The dominant reflection-free facies

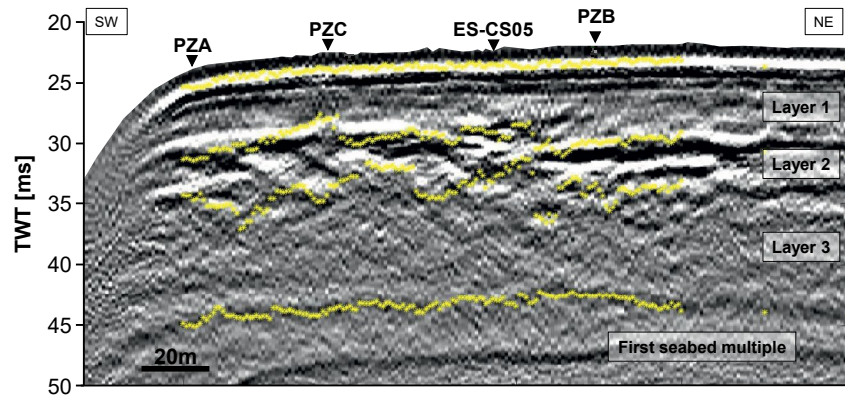


Figure 3. Post-stack constant-velocity migrated seismic section ST5-014. Yellow dots indicate where velocities were picked from the semblance analysis.

is interrupted from about 5 ms two-way travel time (twt) below the seafloor by a package of high-amplitude, locally chaotic reflections. Based on the presence of this package and that of a medium amplitude reflection at 45 ms (twt) three distinct layers can be defined (Figure 3).

The yellow dots presented on the seismic section in Figure 3 show that the peaks picked for the semblance-based velocity analysis were not always horizon consistent. As shown in Figure 4 and Table 2, the interval velocities derived from this analysis reveal a reversal from values above 1,530 m/s in layer 1 to values consistently lower than 1,480 m/s below. With a mean velocity of 1,330 m/s, layer 2 distinguishes from layer 3 which is characterized by a mean velocity of 1,400 m/s (Table 2). Besides, lateral variations of interval velocities are more pronounced in layer 2 than in layer 3 (Figure 4 and Table 2). This is also illustrated in Figure 5 by the depth profiles of velocity extracted at piezometer and coring sites. Considering that these sites were projected on the seismic section from a distance ranging from 2 to 35 m (as indicated in Figure 4), Figure 5 also reveals that piezometer PZ2B reached only the top of layer 2 while piezometers PZ2A and PZC and core ES-CS05 reached layer 3. Analysis of Figure 5 reveals that the uncertainty in interval velocity estimation is inversely proportional to layer thickness. The largest uncertainties range from ± 113 to ± 198 m/s in the 1.8–3.9 m thick layer 2. The lowest uncertainties vary from ± 36 to 60 m/s in the 6.4–7.6 m thick layer 3.

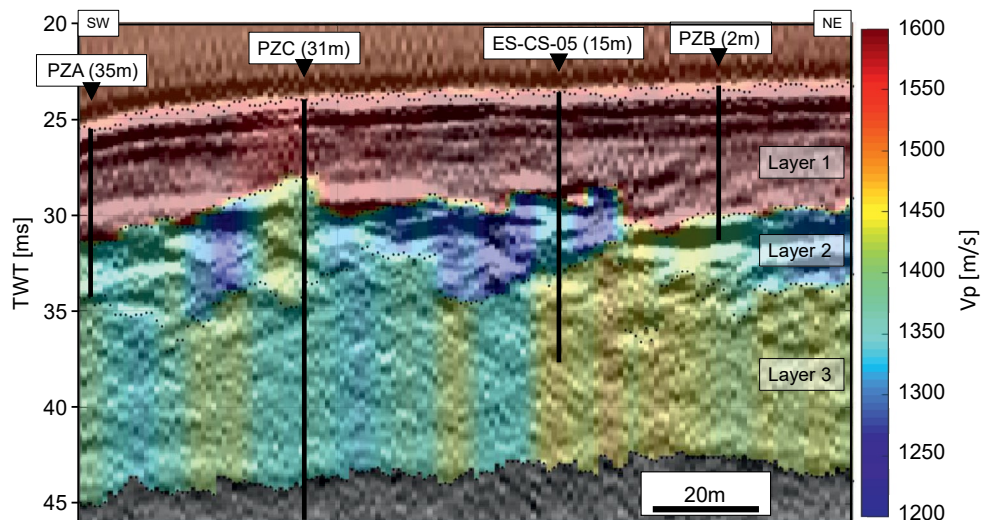


Figure 4. Interval velocities superimposed on the south-western part of seismic section ST5-014. The distance of the piezometer and coring sites to the seismic section are indicated in brackets.

Table 2
Synthesis of the Variations in Interval Velocities of the Three Different Layers Identified on Seismic Section ST5-014

	Min V_p (m/s)	Mean V_p (m/s)	Max V_p (m/s)
Layer 1	1,535	1,585	1,635
Layer 2	1,160	1,330	1,460
Layer 3	1,325	1,400	1,475

4.2. Sediment Core Data

The bulk density of the sediment in core ES-CS05 fluctuates around a mean value of 1.85 g/cm³ except in the upper meter where it is consistently lower than 1.8 g/cm³ (Figure 6). As a consequence, the density profile does not show any clear evolution with depth nor with the position of the three layers identified on seismic data. This contrasts with the decrease in V_p and recurrent loss of acoustic signal (both with the MSCL and ultrasonic fork) beneath the base of layer 1 which is characterized by a mean V_p value of 1,570 m/s (Figure 6). Where measurements were possible, MSCL values are in the order of 1,400 m/s in layer 2. The rare values

measured in layer 3 with the MSCL vary from 1,360 to 1,570 m/s while values obtained with the ultrasonic fork vary from 1,530 to 1,630 m/s (Figure 6). This difference may arise from the better acoustic coupling of the ultrasonic fork compared to the MSCL system. However, since the core liner was observed to be full of sediment, it may also stem from the frequency dependence of V_p in gassy sediments (see Wilkens & Richardson, 1998). That is to say that some bubbles may be detected at the MSCL frequency of 230 kHz but not at 1 MHz frequency with the sonic fork. Visual observations did not reveal the presence of voids, cracks, or fissures that could be unambiguously ascribed to the presence of gas in the predominantly silty clay of core ES-CS05. The predominance of this lithology can be reconciled with the mineralogical analyses which do not reveal any marked changes along the core (Figure 6). Calcite, clay, and quartz dominate the mineralogical composition of the sediment with respective mean proportions of 36%, 31%, and 22%. The mean proportion of plagioclase is slightly higher than 5% while it is around 2.5% for dolomite and K-feldspar and only 0.2% for pyrite. To complete the petro-physical characterization of the sediment, Figure 6 illustrates that the recompression (Cr) and compression (Cc) indices obtained from oedometer tests fluctuate simultaneously without any clear correlation with the position of the three layers identified on seismic data. The same applies to the swelling indices (Cs) which fluctuate slightly around a mean value of 0.013.

Besides, the geochemical analyses of the pore-water reveal a nearly flat chloride profile with concentration values typical of Mediterranean seawater (Figure 7; Oehler et al., 2017). The sulfate profile shows a marked change around the base of layer 1 (Figure 7). Above, sulfate concentrations almost linearly decrease with increasing depth from a value typical of Mediterranean seawater of around 30 mM (Schmidt et al., 2017) to a minimum value of 13 mM. Beneath, in layers 2 and 3, sulfate concentrations are most commonly less than 0.8 mM. Few exceptions can be observed near the base of layer 2 where sulfate concentrations range between 1.4 and 2.4 mM. The profile of DOC in pore-water nearly mirrors the sulfate profile especially

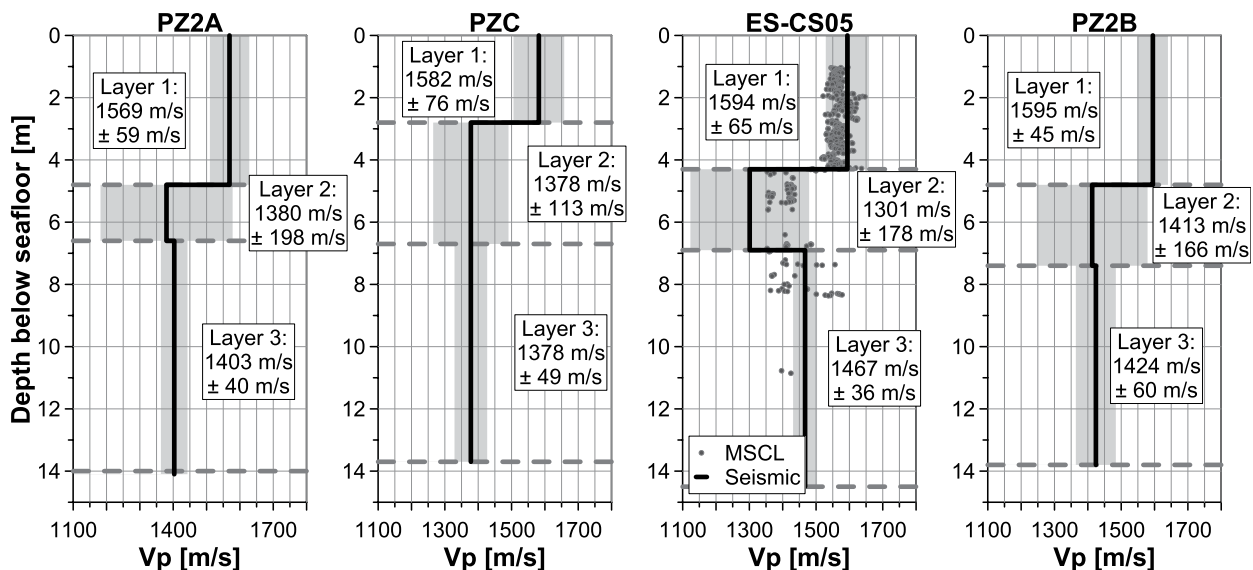


Figure 5. Depth profiles of compressional wave velocity (V_p) extracted at piezometer and coring sites from the velocity field shown in Figure 4. Uncertainties in interval velocity estimates are represented as gray bands. The V_p obtained on core ES-CS05 with the MSCL is also presented.

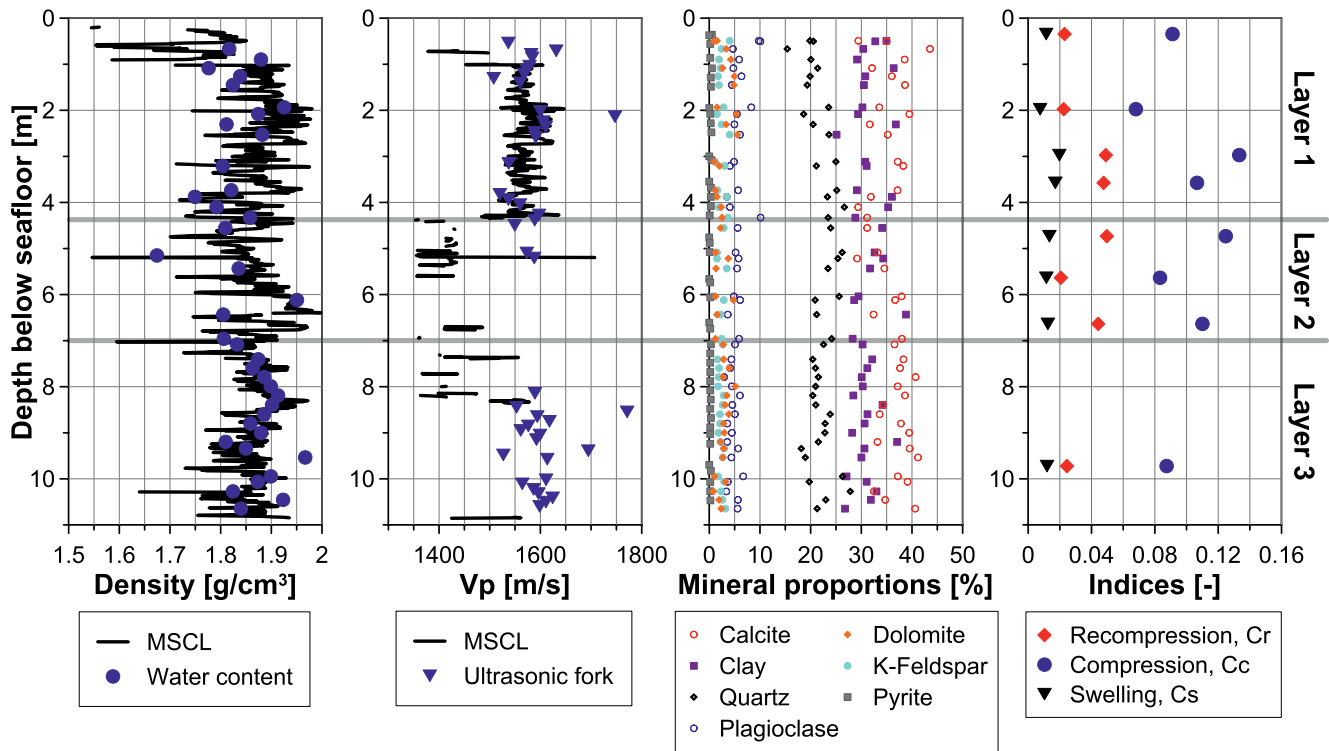


Figure 6. Profiles of bulk density, compressional wave velocity (V_p), mineral proportions, and compressibility properties (recompression, compression, and swelling indices) obtained from oedometer tests on sediment core ES-CS05.

by showing a sharp transition around the base of layer 1. The fraction of TOC measured in bulk sediment displays a different pattern which is characterized by a noticeable increase only around the boundary between layers 1 and 2. Overall, the geochemical profiles of core ES-CS05 compare well with those reported by Schmidt et al. (2017) for the River Rhone delta in the western Mediterranean. There, sulfate depletion

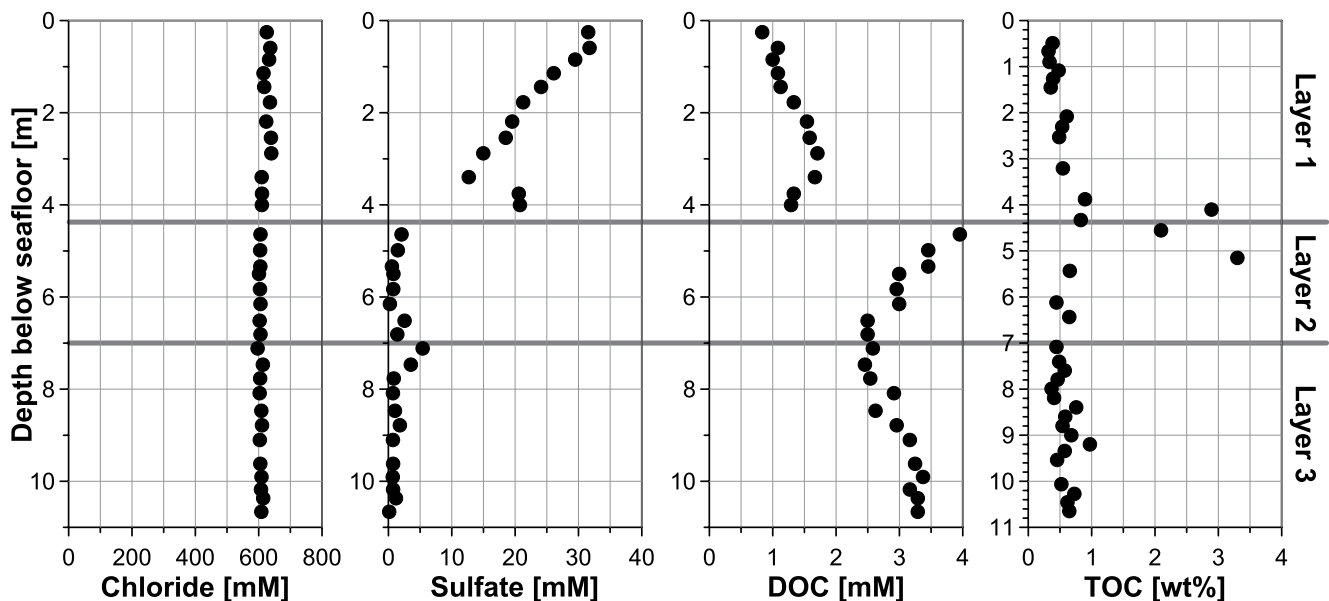


Figure 7. Depth profiles of chloride, sulfate, and dissolved organic carbon (DOC) millimolar (mM) concentrations in pore-water of core ES-CS05. The weight percent of total organic carbon (TOC) presented to the right of the figure were measured in bulk sediment.

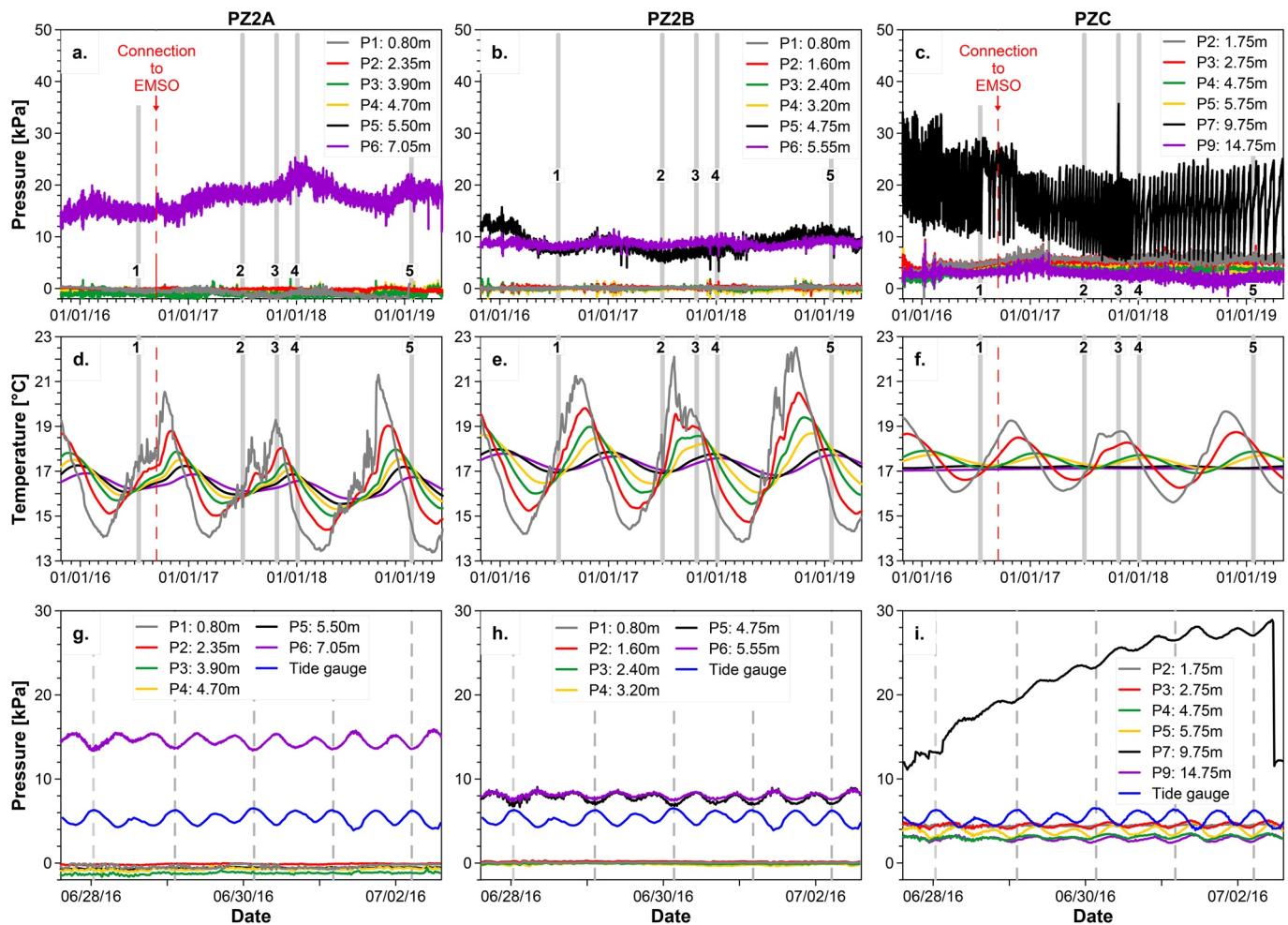


Figure 8. Comparative plots of the pore pressure (a–c) and temperature (d–f) recorded by piezometer PZ2A (left), PZ2B (center), and PZC (right). The gray vertical bars labeled 1–5 indicate periods of particular interest. The dashed red line indicates when two of the piezometers were connected to the cabled EMSO observatory to provide real-time data. The three lower graphs (g–i) compare piezometer pore-pressure records with tidal-pressure records over 5 days around period 1.

(down to 1 mM) is commonly associated with marked increases in dissolved methane concentration above 2 mM.

4.3. Sediment Pore Pressure and Temperature Data

Given the number of piezometer records (Figure 8), it is convenient to first analyze their respective variability over the long term before focusing on fluctuations on the time scale of a complete tidal cycle.

4.3.1. Long-Term Fluctuations in Pore Pressure and Temperature

The upper part of Figure 8 compares the pore pressure and temperature measurements of piezometers PZ2A, PZ2B, and PZC over a common monitoring period of about three and a half years from October 2015 to May 2019. The three piezometers appear to have recorded overpressures of varying magnitude and depth distribution but comparable seasonal temperature fluctuations (Figures 8a–8c). At site PZ2A, overpressures only occurred at the level of sensor P6 located at 7.05 mbsf. Here they fluctuated from around 15 kPa to a maximum of about 23 kPa without any direct relationship to the cyclic changes in temperature between 16 and 17°C (Figure 8a). The same applies to the two deepest levels of PZ2B at 4.75 and 5.55 m below the seafloor, where variations in overpressure from 7 to 12 kPa do not show any appreciable correlation with the cyclic temperature

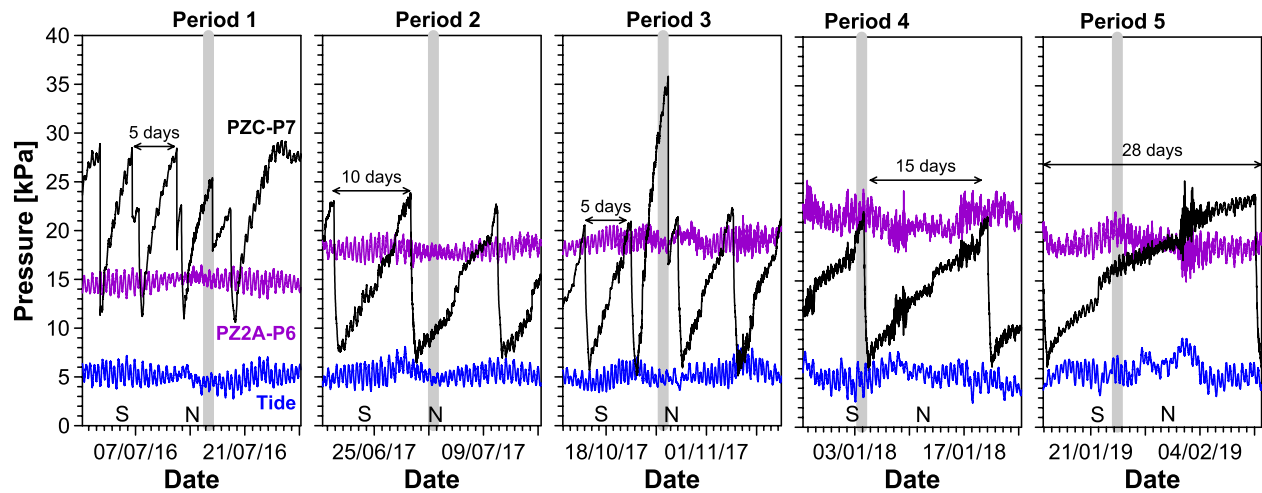


Figure 9. Comparative plots of the tidal pressure and pore pressures recorded by sensor P6 of piezometer PZ2A and sensor P7 of PZC. Each graph covers a 28-day period surrounding the five periods of particular interest discussed in the text and indicated by vertical gray lines. Periods of neap and spring tides are respectively indicated by the letters N and S.

variations in the range 17–18°C. By contrast with PZ2A and PZ2B records, the pore pressures measured by the different sensors of piezometer PZC commonly ranged between 2 and 8 kPa except at P7 location (Figure 8c). Indeed, at 9.75 m depth, sensor P7 recorded recurrent episodes of progressive increases in pressure reaching up to 25 or 30 kPa followed by rapid drops down to 10 or 8 kPa (Figure 8c). As illustrated in Figures 8h and 9, such changes produced a sawtooth signal. The periods of pressure increase varied from around 5 days up to a month while the abrupt decreases occurred over 4 min to several tens of minutes (Figure 9).

Further to this analysis of long-term trends, five periods are distinguished to reflect the temporal variability in overpressure across the three piezometer sites (Figure 8). To serve as a basis for the analysis of the pore pressure response to tidal loading presented below, each period spans a complete tidal cycle (about 25 hr) over a range of neap and spring tides (Figure 9). Figure 9 highlights that the highest fluctuations in overpressure over these five periods range from 7 kPa at the levels of the P6 sensor of PZ2A to up to 24 kPa at that of the P7 sensor of PZC. In Figure 8, these fluctuations mask those on the order of 1 kPa recorded at other sensor levels.

4.3.2. Short-Term Fluctuations in Pore Pressure

The 5-day records of the three piezometers presented in the lower part of Figure 8 emphasize sinusoidal-like fluctuations superimposed on long-term trends in pore pressure. These fluctuations are exclusively expressed at the previously described overpressured levels, that is, from 2.75 to 14.75 mbsf at site PZC, from 4.75 to 5.55 mbsf at site PZ2B and at 7.05 mbsf at site PZ2A (Figure 8). The amplitude of the sinusoidal-like fluctuations varies from one level to the other while they all appear to have a periodicity similar to the tide. A Fourier spectral analysis confirms the measured pore pressure fluctuations have periods associated with the mixed semi-diurnal tide (1 and 2 cycles per day, Figure 10). After the removal of the frequencies lower than 1 cycle per day and higher than 4 cycles per day, comparison of the filtered pore pressure data reveal varying time lags between extrema of pore pressure and tide pressure (Figure 11). At the level of the P6 sensor of PZ2A, the pore pressure signal is most commonly completely (180°) out of phase with that of the tide. The phase lags between tide and pore pressure fluctuations measured by P5 and P6 sensors of piezometer PZ2B are in the order of $180^\circ \pm 20^\circ$ and are thus more variable than those observed for PZ2A (Figure 11). The highest variability is seen at site PZC where phase lags tend to increase with depth from $180^\circ \pm 23^\circ$ at 2.75 mbsf (sensor P3) to $250^\circ \pm 4^\circ$ at 9.75 mbsf (sensor P7).

To complete the picture of the high-frequency pore pressure fluctuations, Figure 12 shows the ratio of their amplitude to that of the tidal pressure fluctuations ($\Delta u/\Delta P$). This ratio appears to vary in a random fashion with depth below the seafloor. Variations of this ratio from 0 to 1.14 are also observed depending on the site and period considered (Figure 12). Overall, the maximum $\Delta u/\Delta P$ ratios are reached during period 4 while the minimum $\Delta u/\Delta P$ ratios are reached during period 1 (Figure 12). It is worth noting that $\Delta u/\Delta P$ is most

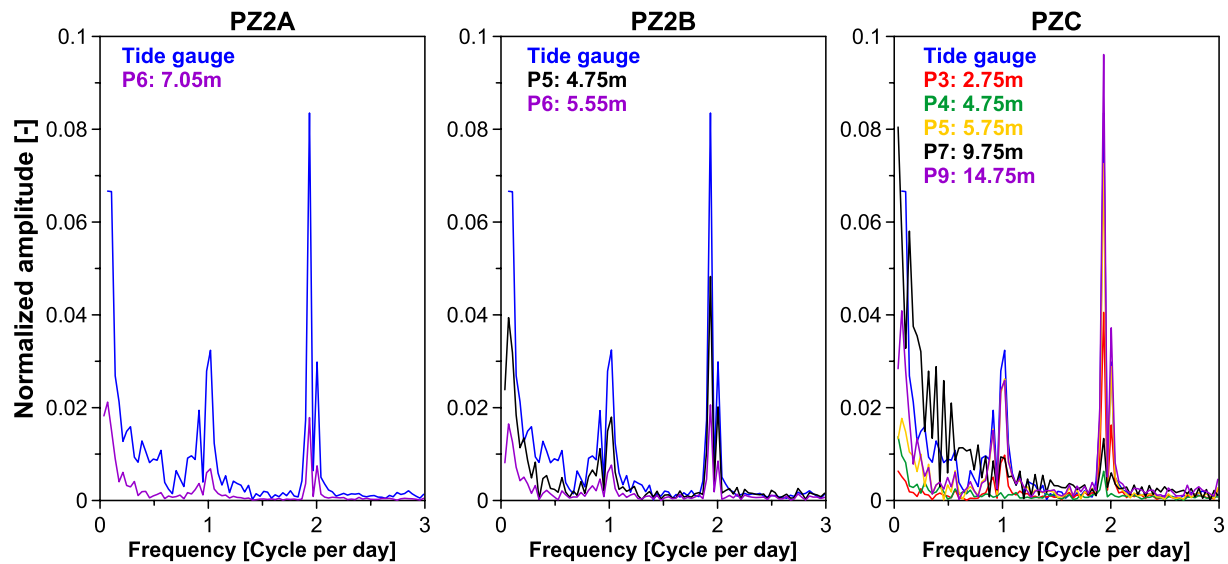


Figure 10. Comparative spectrograms of pore pressure and tide-gauge signals.

commonly higher than 0.9 at the levels of the P6 sensor of PZ2A and of the P5 sensor of PZ2B. This has implications for the estimation of free gas content as indicated in Section 4.5.

4.4. Estimation of Free Gas Content From Seismic Velocities

Following the method presented in Section 3.5, gas volume fractions, n_g , were estimated from interval velocities derived from seismic data, at the sites of the three piezometers (Figures 4 and 5 and $V_{p, \text{seis}}$ in Table 3). The mineralogical composition of the sediment obtained from the XRD analysis of core ES-CS05 (Figure 6) was used as an input parameter to the effective medium model. As shown in Table 3 mineralogical proportions were averaged over the varying thickness of the three layers identified on seismic data. A common value of void ratio at 0.01 kPa vertical effective stress (e_v) and compression index (C_c) was ascribed to the different layers to determine the evolution of porosity and density with depth. These values were taken as the means obtained from oedometer tests on samples from layer 1 which, according to the V_p measured on core sediment (Figure 5), can be considered as representative of fully saturated sediments.

Other calculation parameters included the elastic moduli and density of the minerals and fluids presented in Table 4. As for the type of gas, methane was inferred from the analysis of geochemical profiles obtained

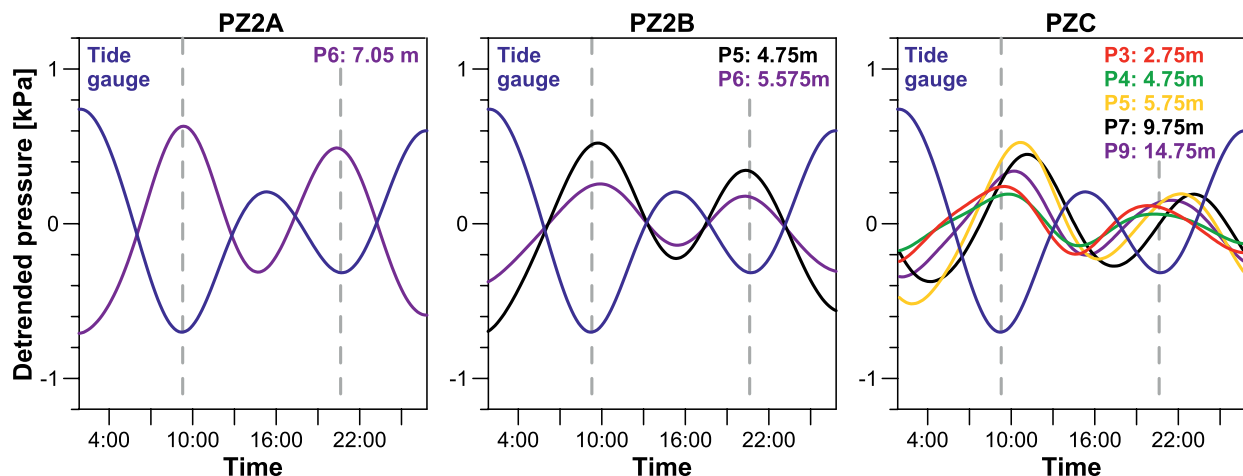


Figure 11. Comparative plots of detrended pore pressure and tidal pressure records over the complete tidal cycle of period 2.

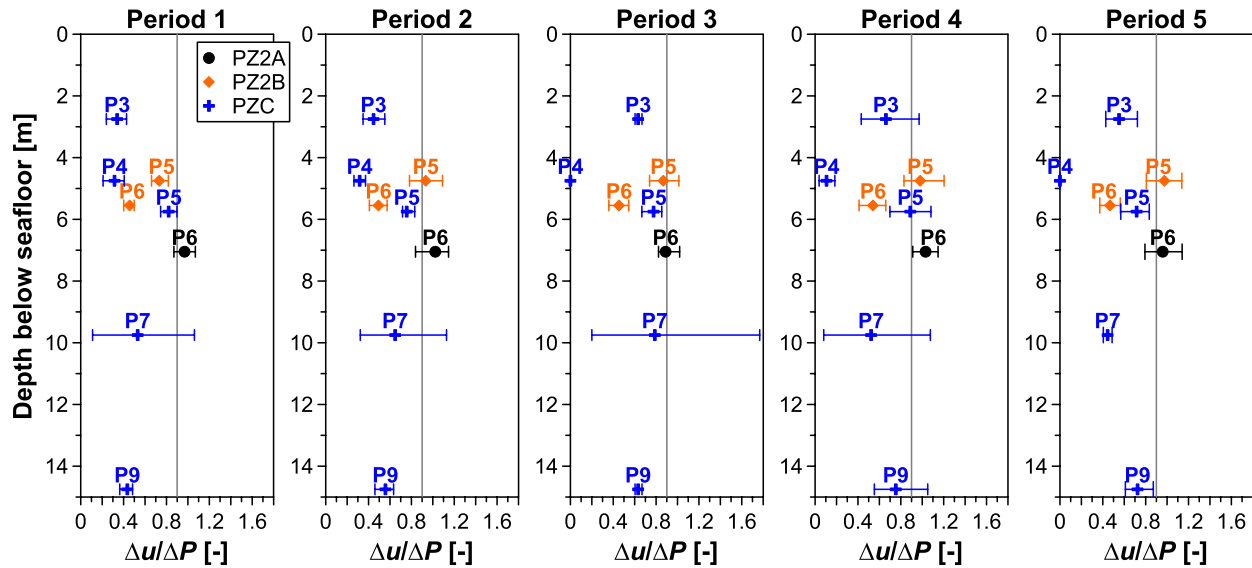


Figure 12. Comparative plots of the ratios of pore pressure amplitude to the tidal pressure amplitude ($\Delta u/\Delta P$) over the complete tidal cycles of periods 1–5.

on core ES-CS05 (Figure 7). Indeed, the marked drop in sulfate concentration to less than 1 mM at about 4 mbsf and coeval changes in DOM are characteristic features of organic-rich continental shelf sediments where methanogenesis begins once sufficient sulfate is removed from pore fluids (Mogollón et al., 2011; Schmidt et al., 2017).

The left-hand graph in Figure 13 illustrates the overall good agreement, in layer 1, between measured densities and the modeled density profile used for the estimation of n_g . By contrast, in layers 2 and 3, measured densities tend to be consistently lower than the calculated ones. This can be reconciled with results in Figure 6 indicating the presence of free gas through reduced V_p in these layers. Accordingly, the modeled density profile is considered as representative of fully water-saturated conditions as required for the fluid substitution procedure.

By considering the uncertainties in interval velocity presented in Figure 5, estimates of n_g in layer 1 vary between 0% and 0.001% for an assumed homogeneous distribution of free gas and between 0% and 0.27%

Table 3
Synthesis of the Input Parameters of the Effective Medium Model

Layer #	Calcite (%)	Clay (%)	Quartz (%)	Plagioclase (%)	Dolomite (%)	Feldspar (%)	Pyrite (%)	e0 (-)	Cc (-)	$V_{p_{seis}}$ (m/s)
PZA										
1	34.97	31.76	21.74	6.03	2.84	2.41	0.24	1.32	0.128	1,569 ± 59
2	34.82	31.76	23.67	5.25	2.22	2.19	0.10	1.32	0.128	1,380 ± 198
3	37.40	30.82	21.86	4.59	2.82	2.31	0.21	1.32	0.128	1,403 ± 40
PZB										
1	34.59	31.93	22.15	5.98	2.80	2.32	0.22	1.32	0.128	1,595 ± 45
2	36.98	31.17	22.29	4.71	2.48	2.21	0.16	1.32	0.128	1,413 ± 166
3	37.08	30.75	22.05	4.76	2.74	2.42	0.21	1.32	0.128	1,424 ± 60
PZC										
1	35.87	31.44	20.64	6.30	3.27	2.24	0.24	1.32	0.128	1,582 ± 76
2	34.60	31.99	23.40	5.22	2.28	2.35	0.17	1.32	0.128	1,378 ± 113
3	37.32	30.70	22.01	4.64	2.74	2.38	0.21	1.32	0.128	1,378 ± 49

Table 4
Elastic Moduli and Density of Sediment Constituents Used as Constants in the Effective Medium Theory (From Mavko et al., 2009)

Constituent	Density, γ (g/cm ³)	Bulk modulus, K (GPa)	Shear modulus, G (GPa)
Calcite	2.71	76.8	32
Clay	2.58	20.9	6.85
Quartz	2.65	36.6	45
Plagioclase	2.63	75.6	25.6
Dolomite	2.87	94.9	45
Feldspar	2.62	37.5	15
Pyrite	4.93	147.4	132.5
Seawater	1,028	2,5	0
Methane	= f(P,T)	= f(P,T)	0

Note. The temperature and pressure-dependent density and adiabatic bulk modulus of methane gas were calculated from equations presented in Batzle and Wang (1992) and Mavko et al. (2009).

if patchy (Figure 13). The difference between estimates obtained with these distinct assumptions is one order of magnitude higher in layers 2 and 3. The assumption of a homogeneous free gas distribution yields estimates of n_g ranging from less than 0.001%–0.008% in layer 2 and from 0.001% to 0.005% in layer 3. As discussed in Section 5.1, such extremely low values cannot be considered as reliable lower bounds of gas content because they were obtained by assuming that bubbles are contained only in the pore fluid space. This is not the case with the patchy assumption from which n_g is estimated to vary from 0.12% to 1.9% in layer 2, whereas they vary less, from 0.44% to 1.44% in layer 3.

4.5. Estimation of Free Gas Content From Piezometer and Tide Gauge Records

As detailed in Section 3.6 the theoretical equilibrium model of Sobkowicz and Morgenstern (1984) was used in the inversion of tidally induced pore pressure fluctuations for estimating sediment saturation. This approach relied on input parameters obtained or inferred from the analysis of sediment core ES-CS05 (Figures 6 and 7). In agreement with the works of Wang et al. (1998), void ratios and swelling indices obtained from oedometer tests were used to account for the elastic compressible

response of sediment to tidal loading. An additional contribution of gas to sediment compressibility was considered by relying on Henry's law solubility constants (H) of methane. As previously explained, methane was inferred from the analysis of geochemical profiles obtained on core ES-CS05 (Figure 7). Based on the nearly flat pore-water chloride profile (Figure 7) and on the relationship between salinity and chlorinity ($S = 1.80655Cl$ from Turekian et al., 2010) a salinity of 39 parts per thousand (ppt) was considered for the selection of Henry's solubility constants adapted to the study area. Additionally, the temperature dependence of the Henry's solubility constants was accounted for by using the expression experimentally derived by Yamamoto et al. (1976).

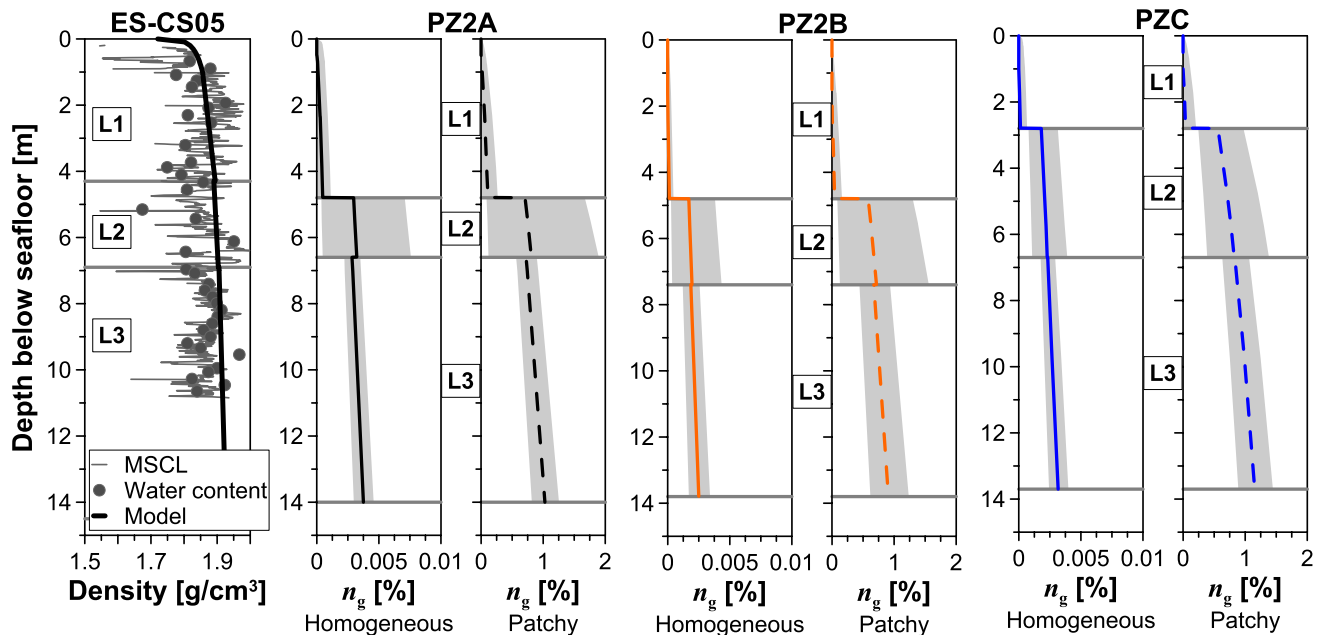


Figure 13. Left: Comparative plots of the bulk density obtained from MSCL and water content on core ES-CS05 together with the density calculated using oedometer results (Model: black curve). Right: Comparison of the gas volume fraction (n_g) estimated from interval velocities at the three piezometer sites by assuming a homogeneous or patchy distribution of free gas in sediment. The solid or dashed lines show the n_g obtained from the initial (i.e., best) estimate of interval velocity while the gray areas indicate the range of values obtained from uncertainties in interval velocity.

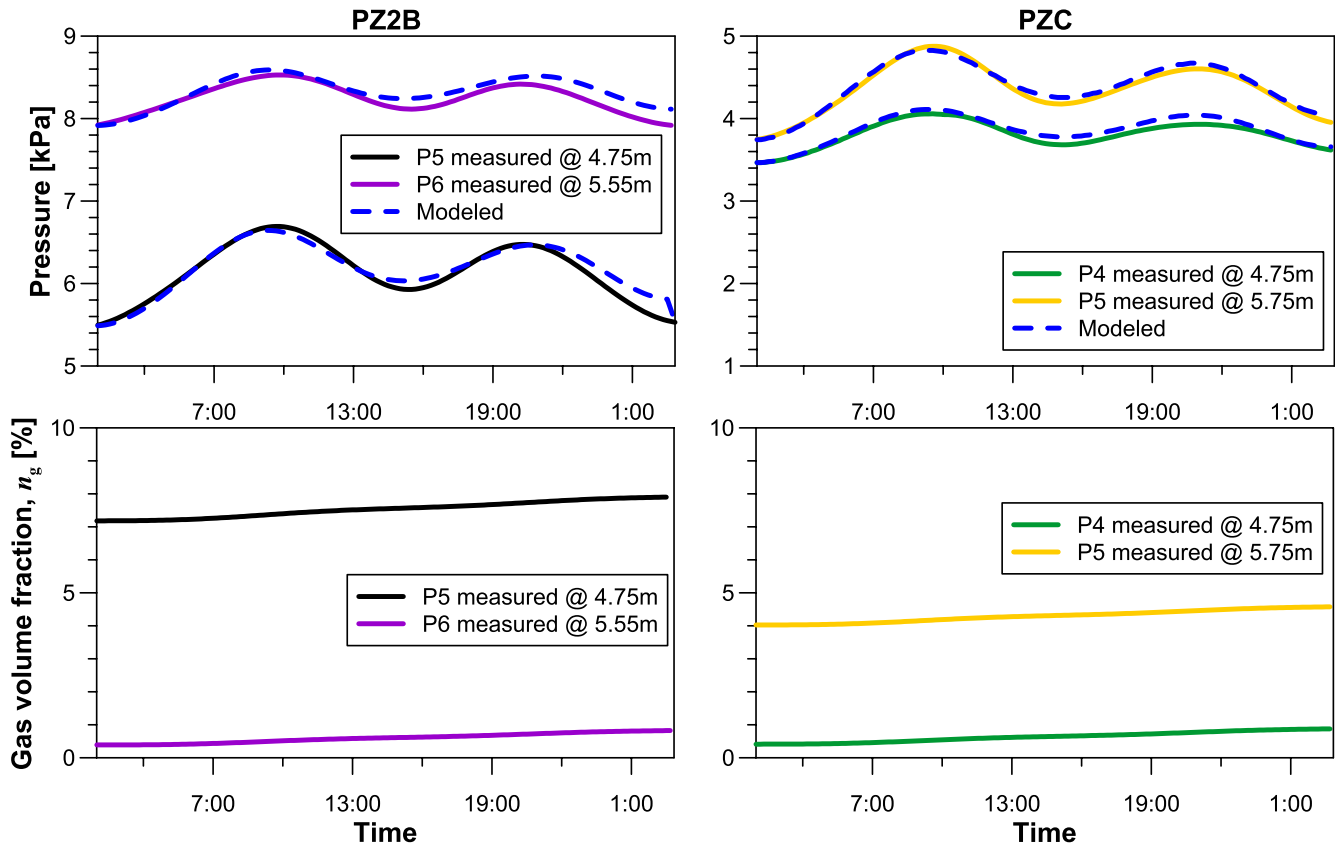


Figure 14. Upper panel: Comparative plots of measured and predicted fluctuations in pore pressure at two similar locations on piezometers PZ2B and PZC during period 2. Lower panel: Comparative plots of model estimations of the gas volume fraction, n_g .

Different initial conditions of vertical effective stress and liquid/gas saturation pressure ($u_{l/g}$) were set to model the pore pressure fluctuations recorded by the different piezometer sensors during each of the five complete tidal cycles referred to as periods 1–5 in Section 4.3. Pore pressure readings at each level and at the beginning of each of these periods were used to determine initial vertical effective stresses. Besides, $u_{l/g}$ was considered as the hydrostatic pressure at high tide at the depth of each sensor. Because each of the five periods was chosen to start at high tide, this is equivalent to assuming that pore water contains the maximum amount of dissolved methane as initial condition. Subsequently, the changes in total stress calculated from tide gauge records together with in situ temperature records determine gas exsolution, dissolution, and expansion. By comparing the predicted pore pressure fluctuations with the measured ones, the model provides an average estimate of free gas content over each complete tidal cycle. In the last step, this first estimate is adjusted by accounting for measured changes in effective stress over each of these five cycles. It is important to mention that to achieve comparable analyses between the different piezometers, the pore pressure fluctuations recorded by PZC have been corrected for phase lags higher than 180° which were not observed on the records of the two others (see Section 4.3.2 and Figure 10).

In the upper panel of Figure 14, the model predictions of the tide-induced pore pressure during period 2 are compared to the measured values at two similar levels of piezometers PZ2B and PZC. This highlights that, overall, the deviations between predictions and measurements were at most in the order of 0.3 kPa. Comparison with the plots presented in the lower panel of Figure 14 illustrates that a progressive increase in n_g of up to 0.7% was commonly obtained as the result of changes in effective stress over each of the five cycles. The range of these increases is reported as error bars in Figure 15 together with the value of n_g averaged over the complete tidal cycles of periods 1–5. Before analyzing this figure, it is important to stress that the results presented in Figure 14 are representative of situations where the mean value of the ratios of pore pressure amplitude to tidal pressure amplitude ($\Delta u/\Delta P$) was lower than 0.9. It corresponds to a threshold above which the model could not converge to provide estimates of free gas saturations.

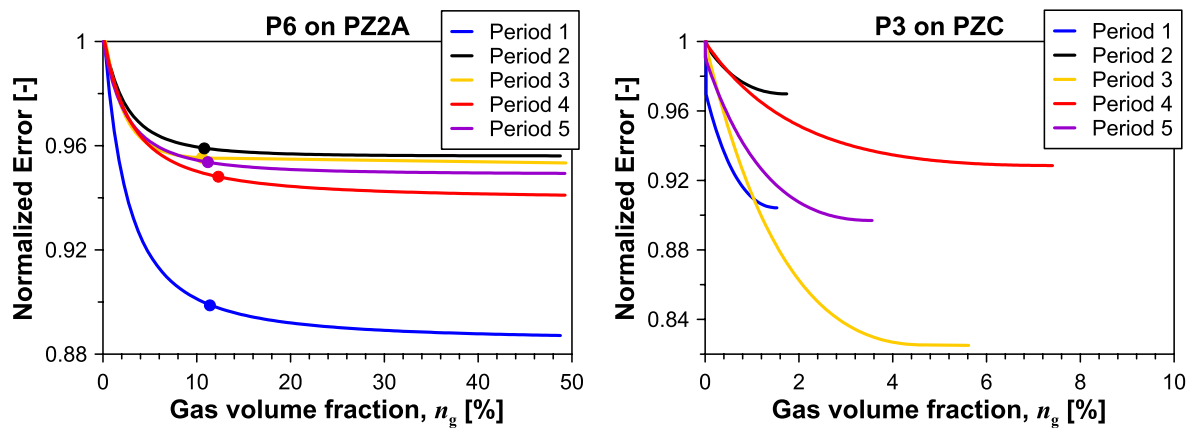


Figure 15. Plots of normalized error versus gas volume fraction, n_g , obtained with the model for five different periods. The circles on the curves correspond to the points of maximum curvature that were used to estimate n_g when model convergence was not achieved.

Examples in Figure 15 illustrate that convergence issues consistently occurred when attempting to estimate free gas saturation from the records of the PZ2A-P6 sensor but never with PZC-P3 records. In an attempt to overcome this issue, n_g was determined as the point of maximum curvature on plots similar to those in Figure 15. Since this always led to estimates of n_g higher than 9.4%, situations when the maximum curvature method was used can be easily detected on the depth profiles in Figure 16.

Hence, the values estimated at the level of sensor PZ2A-P6 (7.05 mbsf) constantly appear as outliers no matter the period (Figure 16). Except for period 2, the same applies to the n_g at the level of sensor PZ2B-P5 (4.75 mbsf). At site PZC, the threshold of 9.4% gas volume fraction has only been reached once, during period 4, at the level of the P5 sensor (5.75 mbsf). Otherwise, n_g values range from 0% to 8.6% and exhibit no trend with depth during periods 1–5 (Figure 16). The scatter with depth evolves over the different periods such that no systematic pattern can be discerned. Comparison of the values obtained at the three piezometer sites in between 4 and 6 mbsf reveals a marked lateral variability but no clear trend.

However, by plotting n_g against overpressure values (u^*) averaged over each of the five different periods, distinct patterns can be discerned. These patterns are here used to define three types of “Free Gas Occurrence” (FGO, left-hand graph in Figure 17). Type 1 FGOs, plot to the left of the graph and show limited changes in

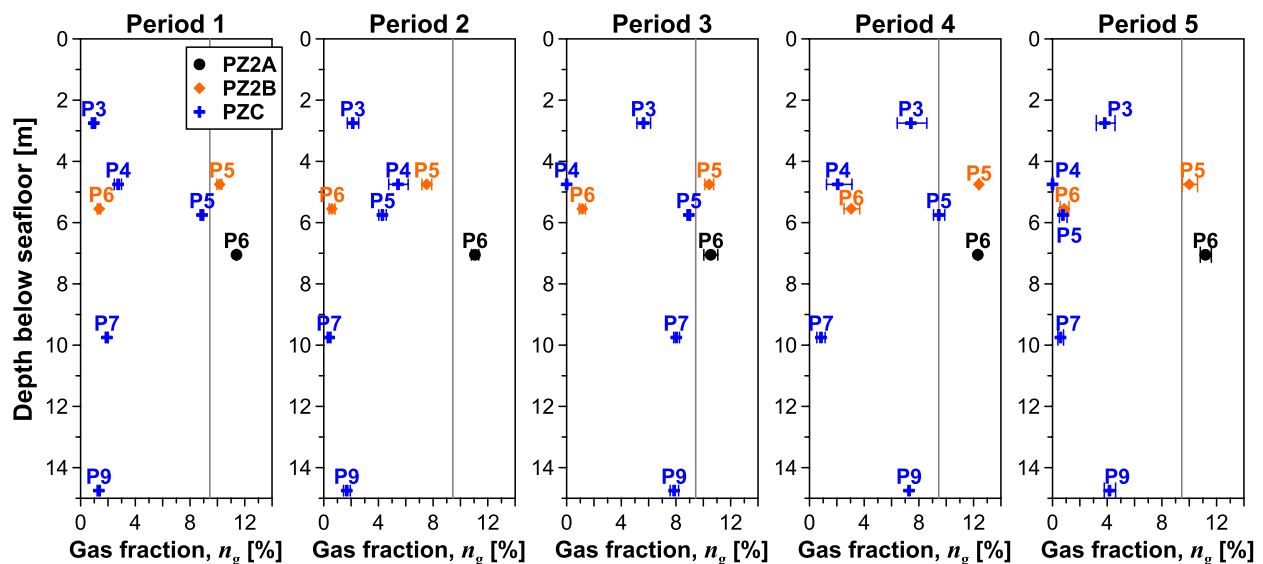


Figure 16. Comparative plots of the fraction of free gas in sediment, n_g , estimated from piezometer and tide gauge records over five different periods. The vertical line corresponds to a threshold of $n_g = 9.4\%$ above which the model fails to converge.

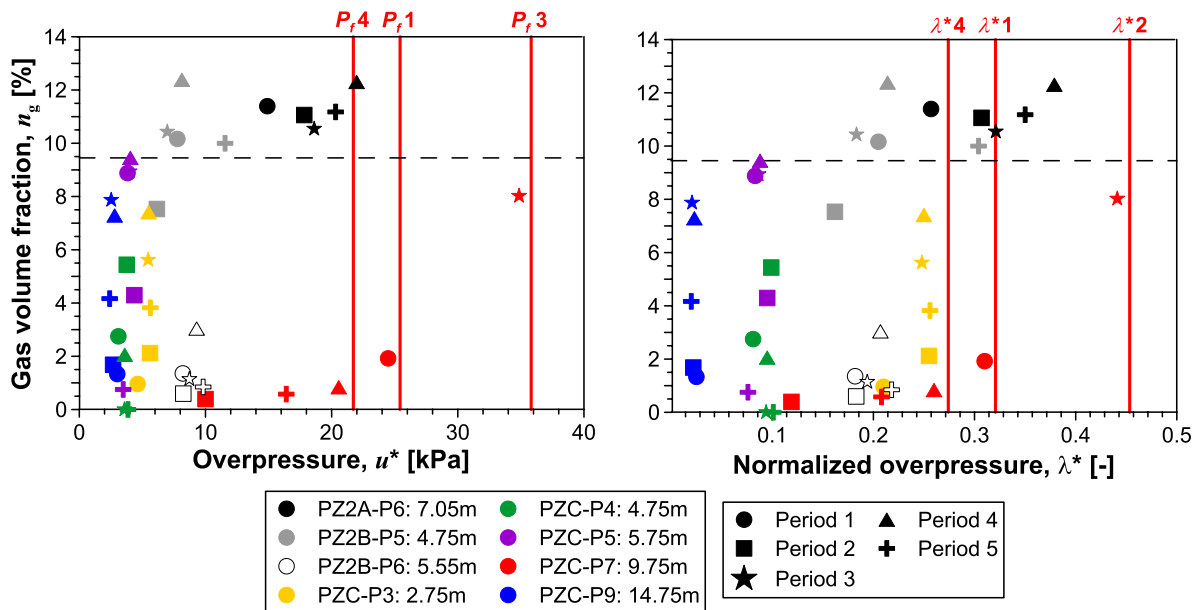


Figure 17. Comparative plots of estimated gas volume fraction, n_g , against: (left) mean overpressures, u^* , (right) mean overpressures normalized to the hydrostatic effective stress, λ^* .

u^* (<3 kPa) but marked changes in n_g in the range (0.38%–3.67%) for PZ2B-P6 to (0.5%–9.9%) for PZC-P5. At the levels of sensors PZ2A-P6 and PZ2B-P5, Type 2 FGOs are characterized by changes in u^* larger than 5 kPa and by n_g values above the previously defined threshold of 9.4%. As discussed hereafter the variability of n_g above this threshold can hardly be interpreted with confidence. The third type of FGO is only detected at the level of the PZC-P7 sensor which recorded sawtooth fluctuations in overpressure ranging in amplitude from 15 kPa (period 4) to 30 kPa (period 3) (Figures 9 and 17). Another characteristic of Type 3 FGO is the variability of n_g which, for periods 1, 3, and 4, appears to scale with the ultimate peak pressure of distinct sawtooth cycles (Figure 17). By analogy with the laboratory results of gas injection in fine-grained cohesive sediment reported by Johnson et al. (2002) or Rocco et al. (2017), these peak pressures preceding rapid falls can be considered as fracturing pressures (P_f). In order to assess their significance to the dynamics of FGOs, the graph to the right in Figure 17 shows overpressure values normalized to the hydrostatic effective stress (λ^*). It highlights that despite the absence of sawtooth fluctuations on PZ2A-P6 and PZ2B-P5 records, λ^* at these sensor locations has reached levels comparable to the P_f recorded by PZC-P7 during periods 1 and 4 (Figure 17).

5. Discussion

The analysis of piezometer data can be synthesized by noting that pore pressure fluctuations of tidal frequencies and varying amplitudes were recorded at different overpressured levels in the upper 2.75–14.75 m of shelf sediments (Figures 8, 9 and 12). In agreement with concurrent observations of reduced seismic velocities within this depth interval, pore pressure fluctuations were considered as indicative of the presence of free gas in fine-grained sediments (Figures 5 and 13). To estimate the amount and distribution of free gas, two different inverse modeling approaches were used (Figures 13 and 16). Before discussing the insights these approaches provide into the dynamics of free gas and the assessment of geohazards in the study area, the next chapter aims at comparing their limitations.

5.1. Limitations of the Geophysical and Geotechnical Modeling Approaches

A large body of literature has examined the different factors which may limit the accuracy of gas-content estimates derived from inverted interval velocity changes (Dogan et al., 2017; Ecker et al., 2000; Tóth et al., 2014; Vardy et al., 2017; Zillmer, 2006; and reference therein). One of the primary limiting factors to

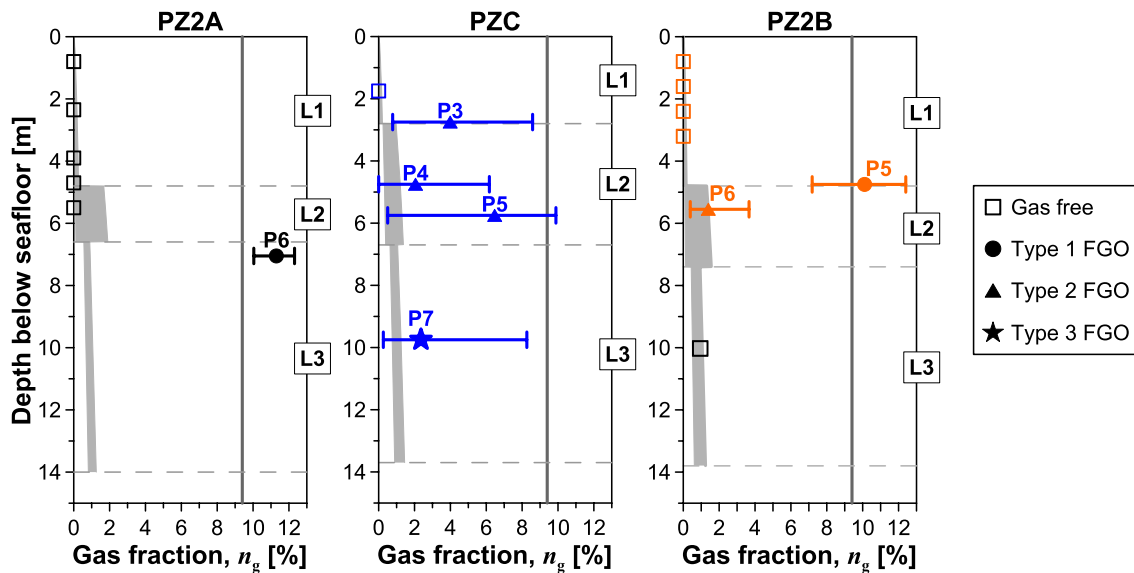


Figure 18. Comparison of n_g estimates derived from seismic and piezometer data. The gray bands represent the uncertainty in n_g estimated from seismic data and the patchy assumption. The symbols and errors bars show, respectively, the average and range of n_g estimated from piezometer data over periods 1–5. The different symbols correspond to the types of free gas occurrence (FGO) shown in the legend to the right.

this approach is related to the spatial resolution of the seismic data and to layer thickness which both influence the picking of velocities (Tóth et al., 2014). In the study area, this implies that the velocity field has a meter-scale horizontal resolution and a vertical resolution (i.e., layer thickness) ranging between 2 and 8 m. Accordingly, n_g values represent averages over volumes of several cubic meters. This warrants caution in comparing estimates derived from seismic data with the centimeter-scale estimates that piezometer data afford. In addition, the former estimates may suffer from uncertainties inherent to the accuracy of interval velocities (Ecker et al., 2000; Tóth et al., 2014; Zillmer, 2006). In this study, the impact of uncertainties in internal velocities is especially marked in the thinnest layer 2 (1.8–3.9 m thick), where they reached up to ± 198 m/s and thus yield a maximum n_g of $1 \pm 0.88\%$ with the patchy assumption (Site PZ2A in Figures 5 and 13). It is noteworthy that even with uncertainties higher than ± 100 m/s in layer 2 (Figure 5), n_g estimates obtained by assuming a homogeneous distribution of free gas are 2 orders of magnitude smaller than the lower bound estimates obtained from the patchy assumption (Figure 13). According to Gardner and Sills (2001) and Mantouka et al. (2016), this is likely due to the inappropriate assumption that bubbles are contained only in the pore fluid space, in the homogeneous distribution case. Theoretical and experimental studies concur to indicate that this is not representative of the structure of fine-grained cohesive sediments in which free gas typically occur in the form of crack-like voids larger than the pore size (Best et al., 2004; Boudreau, 2012; Liu et al., 2016; Rocco et al., 2017; Terzariol et al., 2021). Hence, a patchy distribution of gas bubbles much larger than the sediment pores is best suited to the dominantly silty-clay deposits of the study area. While recognizing that the rock physical model used in this study does not explicitly account for the complexity of compressional wave propagation that can arise when gas bubbles affect the structure of soft sediment (e.g., Leighton, 2007; Mantouka et al., 2016), the synthesis presented in Figure 18 indicates that the patchy assumption yields average n_g estimates of $0.91 \pm 0.7\%$ in layer 2, to $0.93 \pm 0.38\%$ in layer 3. Before discussing how the results obtained with the patchy assumption compare to those obtained from in situ measurements it is worth addressing the limitations of the latter.

Estimates obtained from in situ measurements can be affected by the combination of instrumental and environmental parameters together with model assumptions. The influence of instrumental and environmental parameters is related to the time-dependent load partitioning which Wang et al. (1998) expressed as the loading efficiency. According to the theory they developed, gas fraction determines the decrease in loading efficiency and thus the amplitudes and phases of elastic pore pressures across gas-bearing “interfaces.” Because the application of this theory relies on the quantification of absolute pressure fluctuations in the sediment it is beyond the scope of the present paper. Yet, the results presented by Wang et al. (1998) can be

used to infer that only damped and delayed tidal pressure waves reach levels beneath the first gas-bearing interface. This would explain the piezometer records in Felixstowe silty sediments reported by Thomas and Sills (1990) along with the PZC records here reported. It is worth noting that in Nice as well as in Felixstowe, the shallowest recorded pore pressure fluctuations are completely out of phase (180°) with the tide. Deeper pore pressure records at both sites also attest to increases in phase lag with depth. As of the PZC records, increasing phase lags can be observed down to the P7 sensor location at 9.75 mbsf. Future works are needed to explore if this corresponds to the penetration depth of diffusive pore-pressure waves which, according to Wang et al. (1998), should scale with the square root of hydraulic diffusivity and the tidal period. Meanwhile, it is arguable that, beneath the very top of gas-bearing layer 2, the amplitudes of the recorded pore pressure fluctuations have only yielded lower-bound estimates of n_g . This view is reinforced by the fact that it was always assumed that no free gas was present in the sediment at the beginning of the five distinct periods when applying the model of Sobkowicz and Morgenstern (1984). Additionally, the relevance of this model proved limited to situations where the mean amplitude ratio of pore pressure to tide pressure ($\Delta u/\Delta P$) over each of the five periods considered was lower than 0.9. In the study area, this threshold is related to an n_g of 9.4% or a degree of water saturation, S_r , of 81%. Such a value is close to that of 85% suggested by Nageswaran (1983) as the critical saturation level below which the gas phase becomes continuous and the mechanical response of the sediment departs from that containing small dispersed bubbles. Sobkowicz and Morgenstern (1984) did not consider such a limit and possible changes in matric suction as they derived the theoretical pore pressure response of a soil reaching a S_r as low as $\sim 63\%$ upon isotropic unloading. This can explain the observed convergence issues when using the model with input parameters $\Delta u/\Delta P > 0.9$. Hence, despite the application of the maximum curvature method to try to solve this issue, variations in gas fractions above a threshold of 9.4% are cautiously not considered as representative of the in situ dynamics of free gas. At the same time, because the rated accuracy of pore pressure sensors is in the order of 0.5 kPa, it is possible that gas fractions lower than 0.2% have remained unquantified.

Keeping in mind these limitations and those associated with the inversion of the seismic data, n_g estimates can be compared in Figure 18. As a synthesis of the results presented in Figures 13 and 16, Figure 18 shows the average and range of n_g obtained from in situ measurements over periods 1–5 as solid symbols and error bars, respectively. These are plotted together with the range of n_g obtained by considering uncertainties in interval velocity with the patchy assumption (gray areas) to highlight two distinct situations. The first situation is notably observed at site PZC where error bars indicate that the fluctuation in n_g over the five periods is larger than at the other two piezometer sites. The lowest estimates obtained from PZC pore pressure measurements are consistent with n_g estimated to vary from $0.88\% \pm 0.48\%$, in layer 2, to $1\% \pm 0.4\%$, in layer 3, based on interval velocities (Figure 18). The fact that average values of n_g from PZC measurements plot above this range is possibly due to temporal variations in tidal loading (e.g., Best et al., 2004) and to the dynamics of methane gas (Mogollón et al., 2011) while seismic data were acquired before piezometer installation. Comparison of the different piezometer sites suggests that the first situation is also observed at the level of the P6 sensor of PZ2B, as another characteristic feature of types 1 and 2 FGOs defined in Section 4.5 (Figure 18). This places type 2 FGOs in the second situation where n_g derived from pore pressure measurements vary in a relatively small range that is commonly up to an order of magnitude higher than that determined from seismic data (Figure 18). Such a difference raises the possibility that type 2 FGOs occur over spatial extents too small to be resolved by seismic velocities. In closing this section it is worth acknowledging that pore pressure data suggest that the gas content in shallow shelf sediments vary at a spatial and temporal scale which is inherently difficult to achieve with seismic reflection data. Yet, as discussed in the next section, the results obtained with these two types of data can be combined with geochemical data to draw a broad picture of the distribution and dynamics of free gas in sediment.

5.2. Distribution of Free Gas in Sediment and Underlying Controls

Analysis of the distribution of n_g derived from piezometer data revealed neither clear horizontal nor vertical trends while long-term pore pressure fluctuations bore no evidence of upward fluid flow (Figures 8, 16 and 17). Similar observations can be extrapolated from Figure 19 which shows n_g estimates obtained from inverted interval velocities of the ST5-014 seismic profile and the patchy assumption. While noting that such a variable spatial distribution of free gas is not atypical in organic-rich sediments (Tóth et al., 2014

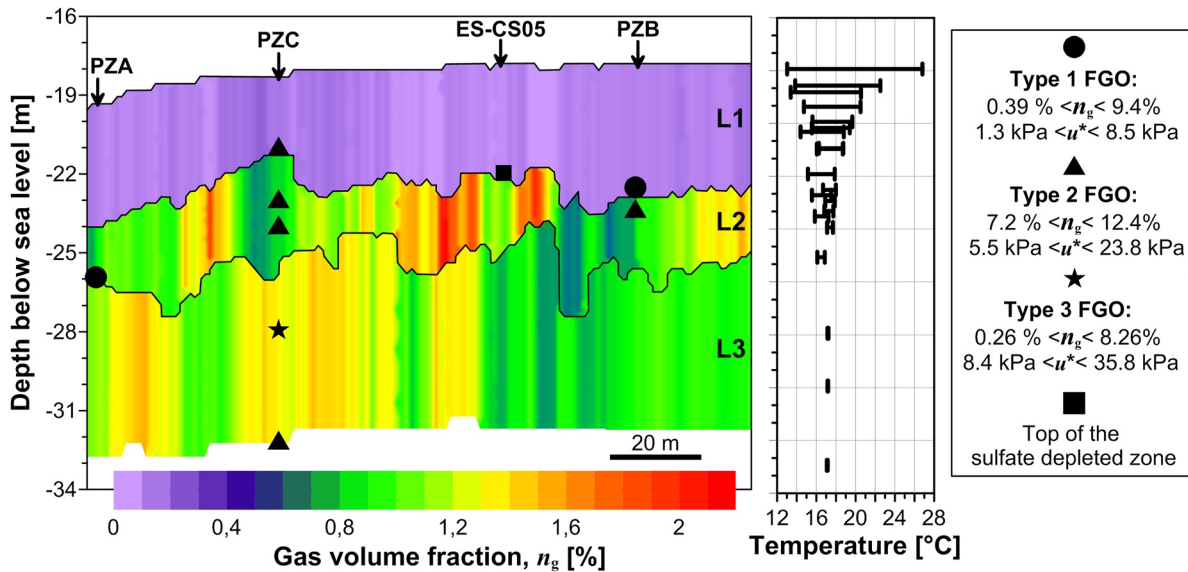


Figure 19. Left: Estimates of gas volume fraction, n_g , derived from ST5-014 seismic data. The three types of free gas occurrence (FGO) as defined by distinctive $n_g; u^*$ (overpressure) relations are indicated by different symbols. The black square at coring site ES-CS05 indicates the top of the sulfate depleted zone identified in Figure 7. The graph to the right shows the full range of temperature fluctuations recorded by piezometers PZ2A, PZ2B, and PZC.

and reference therein), some underlying factors can be discussed with reference to the three types of FGO defined in Section 4.5 (Figure 17).

Analysis of the long-term pore pressure records reveals that sawtooth fluctuations in pressure akin to the process of stable fracture propagation (see Katsman, 2019) are a unique feature of the type 3 FGO at 14.75 mbsf. Hence, by drawing on the conclusions reached by Boudreau (2012) and Acharya et al. (2016), it is the only location where bubble growth and rise can be inferred. Distinguishing between the signatures of these two processes will be the topic of a dedicated study. Meanwhile, it is interesting to note that at the type 3 FGO location n_g appears to scale with the ultimate peak pressure of sawtooth cycles which Acharya et al. (2016) and Rocco et al. (2017) experimentally identified as the “escape pressure” or “fracturing pressure.” To gain some sense of the magnitude of these ultimate peak pressures in the study area, they have been normalized to the hydrostatic effective stress, providing overpressure ratios in the $0.27 < \lambda^* < 0.45$ range. Such values are lower than those considered by different authors at the onset of fracture conduit formation (i.e., $0.6 < \lambda^* < 0.75$ in Daigle & Dugan, 2010; Stranne et al., 2016; Sultan, Marsset, et al., 2010). This is consistent with the findings by Algar et al. (2011) that gas bubbles can more easily form and rise through previously formed, partially annealed fractures. In evaluating the controls on fracturing, it is apparent from Figure 9 that the sawtooth cycles bear no consistent relationships with the tidal cycles nor with the amplitudes of the spring and neap tides. As shown in Figures 8f and 19, the temperature stability at 9.75 mbsf also precludes the possibility of a thermal control. Hence, by considering the sulfate depletion observed beneath the top of layer 2, it is arguable that the dynamics of the type 3 FGO is mainly driven by a locally high rate of methanogenesis. Taken together, the parametric analyses carried out by Algar and Boudreau (2009) and Dale et al. (2009) pointed out that the methane production rate (or source strength) plays a key role in determining the rate of bubble growth and upward gas transport then, in turn, the depth of the gas front below the seafloor. These findings are taken to suggest that the shallowing of the gas front at the PZC site may reflect the high source strength in the surroundings of the type 3 FGO (Figure 19). Interestingly, it is in contrasting sectors where the top of layer two is flat and/or parallel to the seafloor that type 2 FGOs lie (Figure 19). This illustrates that large volumes of free gas in excess of $n_g = 9.4\%$ can accumulate beneath a sediment cover capable of supporting overpressures as high as 41% of the hydrostatic effective stress ($\lambda^* = 0.41$; Figures 17 and 19). The works of Algar and Boudreau (2010) offer an explanation for such a situation whereby bubbles can stop growing as a result of a balance between gas diffusion and the properties of the sediment resisting expansion. According to Johnson et al. (2012), these properties primarily include the tensile fracture toughness of cohesive sediments which increase with consolidation (depth below the seafloor) but tend to decrease

with increasing grain size. The experimental results reported by Liu et al. (2016) also indicate a strong dependence of gas accumulation on pore-size distribution. Such site-specific properties are lacking to point to a likely influence of sediment heterogeneity on the spatial variability of gas content and overpressure distribution in sediments. However, in agreement with the observations by Algar and Boudreau (2010), the analysis of the pore pressure response to tidal loading suggests that tides in Nice are insufficient to increase the growth rate of bubbles through the process of rectified diffusion. Accordingly, FGOs of types 1 and 2 are interpreted to be in a “no-growth” condition (*sensu* Algar & Boudreau, 2010), the persistence of which remains to be thoroughly assessed through a dedicated study and longer-term monitoring.

5.3. Geohazard Implications

Through an extensive literature review Kaminski et al. (2020) point out the mechanisms by which gas exsolution and subsequent accumulation of bubbles can affect the stability of submarine slopes. The results of the present study add to the rare *in situ* evidences that free gas migration and accumulation in shallow, fine-grained sediments or peat are associated with transient overpressures (Acharya et al., 2016; Bennett et al., 1996; Tjelta et al., 2007). Because the development of overpressures decreases the effective stress and in turn the resistance to failure (e.g., Stigall & Dugan, 2010), it is worth stressing that λ^* locally exceeds 0.3 in types 2 and 3 FGOs. Indeed, based on the monitoring of artesian groundwater rises, just 10 m deeper in the sedimentary column, Sultan et al. (2020) point out that, a λ^* of 0.28 is sufficient to reduce the factor of safety against shear failure to unity where the slope is steeper than 20° . The fact that such a situation occurs at the level of the P6 sensor of PZ2A suggests that shear failure may initiate from the shelf edge (Figures 1, 17 and 19).

In the absence of any upward pressure gradient between the depth interval studied by Sultan et al. (2020) and the one on which this paper is centered, it is possible to argue that gas charging and focused groundwater flow are two active processes contributing to the initiation of shear zones at different levels. Nevertheless, the high-frequency patterns which can be discerned on the deep overpressure records reported by Sultan et al. (2020) deserve to be analyzed to evaluate the extent to which gas charging is affecting the susceptibility of shelf edge sediments to local failure and in turn to global slope failure. From another perspective, it is anticipated that inversion of the whole seismic data set covering the shelf could yield n_g estimates of relevance to the characterization of the earthquake response of sediments. There is indeed a wide recognition that by increasing pore-fluid compressibility free gas reduces excess pore pressure build-up during earthquake loading (DeJong et al., 2014 and reference therein). Hence, despite the strong site effect revealed by Courbouloux et al. (2020), questions remain as to the possibility that the presence of gas mitigates the earthquake-induced liquefaction potential that Roesner et al. (2019) has stressed.

6. Conclusion

The combination of seismic data with long-term pore pressure records indicated the presence of free gas in the upper 2.75–14.75 m of cohesive, silty-clay sediments covering the shelf offshore Nice Airport. This stems from the concurrent observations of reduced compressional wave velocities and tidal pore pressure fluctuations. The compressibility provided by a gaseous phase in the sediments was considered to estimate gas volume fractions through two complementary inverse modeling approaches. The first one relied on interval velocity changes and a rock-physics model to obtain estimates, by assuming respectively that gas is homogeneously distributed in the pore space or that it occurs in patches larger than the average pore size. Of these two assumptions, the one which entails a patchy distribution of gas bubbles was considered as the best suited to the dominantly silty-clay deposits of the study area. It yielded estimates of gas volume fractions ranging on average from $0.91\% \pm 0.7\%$ to $0.93\% \pm 0.38\%$ in two distinct layers. These turned out to be closer to those obtained by inverting the pore pressure response to tidal loading. However, by considering this response at eight different sensor locations over five distinct tidal cycles, gas volume fractions were estimated to vary from 0.26% to more than 9.4% without showing any systematic pattern with depth and time. It is thus perceived that pore pressure measurements reveal spatio-temporal heterogeneities in free gas content of shallow cohesive sediments which can hardly be resolved and extrapolated using seismic data. In an attempt to characterize further these heterogeneities, three contrasting types of FGO were distinguished

based on relationships between gas volume fractions and overpressure levels. The most striking (type 3) is characterized by sawtooth fluctuations in overpressure of up to 30 kPa in amplitude. It was recognized as the unique manifestation of gas bubble growth and rise through fracturing as the ratio of overpressure to hydrostatic effective vertical stress (overpressure ratio) ranges from 0.27 to 0.45. The possibility that this process attests to a locally high rate of gas production is supported by the shallowing of the gas front at the same location. By contrast with the type 3 FGO, the other two types are characterized by long-term overpressure trends indicative of a situation whereby bubble growth has ceased. Type 1 FGOs are more common and can be distinguished from Type 2 FGOs by their gas volume fraction lower than 9.4% and overpressure ratio lower than 0.3. Type 2 FGOs provide evidences that volumes of free gas in excess of 9.4% can accumulate beneath a sediment cover capable of supporting an overpressure ratio of up to 0.41. By analogy with a recent slope stability analysis, the presence of a type 2 FGO with such characteristics can lead to the initiation of shear failure where the shelf edge is bordered by a slope as steep as 40°.

Beyond its implications for the characterization of active processes in the study area, the distinction of different types of FGO based on their overpressure ratio provides field evidences and testable implications relevant to the dynamics of methane in surficial cohesive marine sediments.

Data Availability Statement

The seismic data presented in this study can be freely downloaded from <https://doi.org/10.17882/82986>. In accordance with EMSO dissemination policy, the data from piezometers connected to the EMSO Ligure Nice cabled observatory can be freely downloaded from <https://www.emso-fr.org/EMSO-Ligure-Nice/Data-download>.

Acknowledgments

This study was variously supported by the EU project EMSO (<http://www.emso-eu.org/>), the “Laboratoire d’Excellence” LabexMER (ANR-10-LABX-19) and, the MODAL project (ANR-17-CE01-0017; <http://modal-project.cnrs.fr/>) funded by the Agence Nationale de la Recherche (ANR) and the Deutsche Forschungsgemeinschaft (DFG, Grant KO 2108/26-1) in the framework of a Franco-German research program. The authors are grateful to the captains and crews of the R/V *L’Europe* and R/V *Pourquoi Pas?*, for their assistance at sea during the STEP 2014 cruise ([doi.org:10.17600/14005400](https://doi.org/10.17600/14005400)), the STEP 2015 cruise ([doi.org:10.17600/15006100](https://doi.org/10.17600/15006100)), and the ESSPENF50 2015 cruise ([doi.org:10.17600/15010900](https://doi.org/10.17600/15010900)). Special thanks go to P. Pelleau, M. Roudaut, A. Ferrant, and P. Guyavarch for ensuring the success of the piezometer monitoring program. Thanks are extended to Stephane Barbot for network handling, to Sandrine Cheron for mineralogical analysis, and to Jérémie Gouriou for organic matter and grain size analyses.

References

- Acharya, M. P., Hendry, M. T., & Martin, C. D. (2016). Effect of gas bubbles on pore pressure response in peat beneath a railway embankment. *Canadian Geotechnical Journal*, 53(5), 765–772. <https://doi.org/10.1139/cgj-2015-0122>
- Algar, C. K., & Boudreau, B. P. (2009). Transient growth of an isolated bubble in muddy, fine-grained sediments. *Geochimica et Cosmochimica Acta*, 73(9), 2581–2591. <https://doi.org/10.1016/j.gca.2009.02.008>
- Algar, C. K., & Boudreau, B. P. (2010). Stability of bubbles in a linear elastic medium: Implications for bubble growth in marine sediments. *Journal of Geophysical Research: Earth Surface*, 115(F3). <https://doi.org/10.1029/2009jf001312>
- Algar, C. K., Boudreau, B. P., & Barry, M. A. (2011). Release of multiple bubbles from cohesive sediments. *Geophysical Research Letters*, 38(8). <https://doi.org/10.1029/2011gl046870>
- Anderson, A. L., & Hampton, L. D. (1980). Acoustics of gas-bearing sediments. II. Measurements and models. *Journal of the Acoustical Society of America*, 67(6), 1890–1903. <https://doi.org/10.1121/1.384454>
- Anthony, E. J., & Julian, M. (1997). The 1979 Var Delta landslide on the French Riviera: A retrospective analysis. *Journal of Coastal Research*, 27–35.
- ASTM. D. (2011). Standard test methods for one-dimensional consolidation properties of soils using incremental loading. In D2435/D2435M-11.
- Barrett, B. J., Huws, D. G., Booth, A. D., Wergeland, Ø., & Green, J. A. M. (2017). Tuning, interference and false shallow gas signatures in geohazard interpretations: Beyond the “λ/4” rule. *Near Surface Geophysics*, 15(4), 359–366. <https://doi.org/10.3997/1873-0604.2017023>
- Batzle, M., & Wang, Z. (1992). Seismic properties of pore fluids. *Geophysics*, 57(11), 1396–1408. <https://doi.org/10.1190/1.1443207>
- Bennett, R. H., Hulbert, M. H., Meyer, M. M., Lavoie, D. M., Briggs, K. B., Lavoie, D. L., et al. (1996). Fundamental response of pore-water pressure to microfabric and permeability characteristics: Eckernförde Bay. *Geo-Marine Letters*, 16(3), 182–188. <https://doi.org/10.1007/BF01204507>
- Best, A. I., Tuffin, M. D. J., Dix, J. K., & Bull, J. M. (2004). Tidal height and frequency dependence of acoustic velocity and attenuation in shallow gassy Marine sediments. *Journal of Geophysical Research*, 109, B08101. <https://doi.org/10.1029/2003JB002748>
- Bompais, X., Garziglia, S., Blandin, J., & Hello, Y. (2019). EMSO-Ligure Nice, a coastal cabled observatory dedicated to the study of slope stability. In OCEANS 2019—Marseille, 1–8. IEEE. <https://doi.org/10.1109/OCEANSE.2019.8867040>
- Boudreau, B. P. (2012). The physics of bubbles in surficial, soft, cohesive sediments. *Marine and Petroleum Geology*, 38(1), 1–18. <https://doi.org/10.1016/j.marpetgeo.2012.07.002>
- Cevatoglu, M., Bull, J. M., Vardy, M. E., Gernon, T. M., Wright, I. C., & Long, D. (2015). Gas migration pathways, controlling mechanisms and changes in sediment acoustic properties observed in a controlled sub-seabed CO₂ release experiment. *International Journal of Greenhouse Gas Control*, 38, 26–43. <https://doi.org/10.1016/j.ijggc.2015.03.005>
- Chéron, S., Etoubleau, J., Bayon, G., Garziglia, S., & Boissier, A. (2016). Focus on sulfur count rates along marine sediment cores acquired by XRF Core Scanner. *X-Ray Spectrometry*, 45(5), 288–298. <https://doi.org/10.1002/xrs.2704>
- Colin, F., Ker, S., & Marsset, B. (2020). Fine-scale velocity distribution revealed by datuming of very-high-resolution deep-towed seismic data: Example of a shallow-gas system from the western Black Sea. *Geophysics*, 85(5), B181–B192. <https://doi.org/10.1190/geo2019-0686.1>
- Courboux, F., Mercerat, E. D., Deschamps, A., Migeon, S., Baques, M., Larroque, C., et al. (2020). Strong site effect revealed by a new broadband seismometer on the continental shelf offshore Nice Airport (Southeastern France). *Pure and Applied Geophysics*, 177(7), 3205–3224. <https://doi.org/10.1007/s00024-019-02408-9>

- Daigle, H., & Dugan, B. (2010). Origin and evolution of fracture-hosted methane hydrate deposits. *Journal of Geophysical Research*, 115(B11). <https://doi.org/10.1029/2010jb007492>
- Dale, A. W., Regnier, P., Cappellen, P. V., Fossing, H., Jensen, J. B., & Jørgensen, B. B. (2009). Remote quantification of methane fluxes in gassy marine sediments through seismic survey. *Geology*, 37(3), 235–238. <https://doi.org/10.1130/G25323A.1>
- Dan, G., Sultan, N., & Savoye, B. (2007). The 1979 Nice harbour catastrophe revisited: Trigger mechanism inferred from geotechnical measurements and numerical modelling. *Marine Geology*, 245(1–4), 40–64. <https://doi.org/10.1016/j.margeo.2007.06.011>
- DeJong, J. T., Soga, K., Kavazanjian, E., Burns, S., Van Paassen, L. A., Al Qabany, A., et al. (2014). Biogeochemical processes and geotechnical applications: Progress, opportunities and challenges. In L. Laloui (Eds.), *Bio-and chemo-mechanical processes in geotechnical engineering: Géotechnique Symposium in Print 2013* (pp. 143–157). Ice Publishing. <https://doi.org/10.1680/bcmapge.60531.014>
- Dogan, H., White, P. R., & Leighton, T. G. (2017). Acoustic wave propagation in gassy porous marine sediments: The rheological and the elastic effects. *Journal of the Acoustical Society of America*, 141(3), 2277–2288. <https://doi.org/10.1121/1.4978926>
- Dvorkin, J., Prasad, M., Sakai, A., & Lavoie, D. (1999). Elasticity of marine sediments: Rock physics modeling. *Geophysical Research Letters*, 26(12), 1781–1784. <https://doi.org/10.1029/1999gl900332>
- Ecker, C., Dvorkin, J., & Nur, A. M. (2000). Estimating the amount of gas hydrate and free gas from marine seismic data. *Geophysics*, 65(2), 565–573. <https://doi.org/10.1190/1.1444752>
- Egger, M., Riedinger, N., Mogollón, J. M., & Jørgensen, B. B. (2018). Global diffusive fluxes of methane in marine sediments. *Nature Geoscience*, 11(6), 421–425. <https://doi.org/10.1038/s41561-018-0122-8>
- Fleischer, P., Orsi, T., Richardson, M., & Anderson, A. (2001). Distribution of free gas in marine sediments: A global overview. *Geo-Marine Letters*, 21(2), 103–122. <https://doi.org/10.1007/s003670100072>
- Fredlund, D. G. (1976). Density and compressibility characteristics of air–water mixtures. *Canadian Geotechnical Journal*, 13(4), 386–396. <https://doi.org/10.1139/t76-040>
- Gardner, T. N. (1999). An acoustic study of soils that model seabed sediments containing gas bubbles. *Journal of the Acoustical Society of America*, 107(1), 163–176. <https://doi.org/10.1121/1.428298>
- Gardner, T. N., & Sills, G. C. (2001). An examination of the parameters that govern the acoustic behavior of sea bed sediments containing gas bubbles. *Journal of the Acoustical Society of America*, 110(4), 1878–1889. <https://doi.org/10.1121/1.1388005>
- Garziglia, S., Woerther, P., Apprioual, R., Roudaut, M., Bompais, X., & Barbot, S. (2018a). *Pore pressure and temperature data from piezometer ST4-PZ2L-01B on EMSO-LIGURE NICE observatory*. SEANO. <https://doi.org/10.17882/51490>
- Garziglia, S., Woerther, P., Apprioual, R., Roudaut, M., Bompais, X., & Barbot, S. (2018b). *Pore pressure and temperature data from piezometer SPF-PZ3L-01C on EMSO-LIGURE NICE observatory*. SEANO. <https://doi.org/10.17882/51528>
- Guglielmi, Y., & Prieur, L. (1997). Locating and estimating submarine freshwater discharge from an interstitial confined coastal aquifer by measurements at sea: Example from the lower Var Valley, France. *Journal of Hydrology*, 190(1–2), 111–122. [https://doi.org/10.1016/S0022-1694\(96\)03061-2](https://doi.org/10.1016/S0022-1694(96)03061-2)
- Hajnal, Z., & Sereda, I. T. (1981). Maximum uncertainty of interval velocity estimates. *Geophysics*, 46, 1543–1547. <https://doi.org/10.1190/1.1441160>
- Helgerud, M. B., Dvorkin, J., Nur, A., Sakai, A., & Collett, T. (1999). Elastic-wave velocity in marine sediments with gas hydrates: Effective medium modeling. *Geophysical Research Letters*, 26(13), 2021–2024. <https://doi.org/10.1029/1999gl900421>
- Johnson, B. D., Barry, M. A., Boudreau, B. P., Jumars, P. A., & Dorgan, K. M. (2012). In situ tensile fracture toughness of surficial cohesive marine sediments. *Geo-Marine Letters*, 32, 39–48. <https://doi.org/10.1007/s00367-011-0243-1>
- Johnson, B. D., Boudreau, B. P., Gardiner, B. S., & Maass, R. (2002). Mechanical response of sediments to bubble growth. *Marine Geology*, 187(3), 347–363. [https://doi.org/10.1016/S0025-3227\(02\)00383-3](https://doi.org/10.1016/S0025-3227(02)00383-3)
- Kaminski, P., Urlaub, M., Grabe, J., & Berndt, C. (2020). Geomechanical behaviour of gassy soils and implications for submarine slope stability: A literature analysis. *Geological Society, London, Special Publications*, 500(1), 277–288. <https://doi.org/10.1144/SP500-2019-149>
- Katsman, R. (2019). Methane bubble escape from gas horizon in muddy aquatic sediment under periodic wave loading. *Geophysical Research Letters*, 46(12), 6507–6515. <https://doi.org/10.1029/2019gl083100>
- Kelner, M., Migeon, S., Tric, E., Coubolex, F., Dano, A., Lebourg, T., & Taboada, A. (2016). Frequency and triggering of small-scale submarine landslides on decadal timescales: Analysis of 4D bathymetric data from the continental slope offshore Nice (France). *Marine Geology*, 379, 281–297. <https://doi.org/10.1016/j.margeo.2016.06.009>
- Ker, S., Thomas, Y., Riboulot, V., Sultan, N., Bernard, C., Scalabrin, C., et al. (2019). Anomalously deep BSR related to a transient state of the gas hydrate system in the western Black Sea. *Geochemistry, Geophysics, Geosystems*, 20(1), 442–459. <https://doi.org/10.1029/2018gc007861>
- Kopf, A. J., Stegmann, S., Garziglia, S., Henry, P., Dennielou, B., Haas, S., & Weber, K.-C. (2016). Soft sediment deformation in the shallow submarine slope off Nice (France) as a result of a variably charged Pliocene aquifer and mass wasting processes. *Sedimentary Geology*, 344, 290–309. <https://doi.org/10.1016/j.sedgeo.2016.05.014>
- Leighton, T. G. (2007). Theory for acoustic propagation in marine sediment containing gas bubbles which may pulsate in a non-stationary nonlinear manner. *Geophysical Research Letters*, 34(17). <https://doi.org/10.1029/2007gl030803>
- Leighton, T. G., & Robb, G. B. N. (2008). Preliminary mapping of void fractions and sound speeds in gassy marine sediments from subbottom profiles. *Journal of the Acoustical Society of America*, 124(5), EL313–EL320. <https://doi.org/10.1121/1.2993744>
- Leynaud, D., & Sultan, N. (2010). 3-D slope stability analysis: A probability approach applied to the Nice slope (SE France). *Marine Geology*, 269(3–4), 89–106. <https://doi.org/10.1016/j.margeo.2009.12.002>
- Liu, L., Wilkinson, J., Koca, K., Buchmann, C., & Lorke, A. (2016). The role of sediment structure in gas bubble storage and release. *Journal of Geophysical Research: Biogeosciences*, 121(7), 1992–2005. <https://doi.org/10.1002/2016jg003456>
- Mantouka, A., Dogan, H., White, P. R., & Leighton, T. G. (2016). Modelling acoustic scattering, sound speed, and attenuation in gassy soft marine sediments. *Journal of the Acoustical Society of America*, 140(1), 274–282. <https://doi.org/10.1121/1.4954753>
- Martín Míguez, B., Le Roy, R., & Wöppelmann, G. (2008). The use of radar tide gauges to measure variations in sea level along the French coast. *Journal of Coastal Research*, 24, 61–68. <https://doi.org/10.2112/06-0787.1>
- Mavko, G., Mukerji, T., & Dvorkin, J. (2009). *The rock physics handbook: Tools for seismic analysis of porous media*. Cambridge University Press.
- Mei, C. C., & Foda, M. A. (1981). Wave-induced responses in a fluid-filled poro-elastic solid with a free surface, a boundary layer theory. *Geophysical Journal International*, 66(3), 597–631. <https://doi.org/10.1111/j.1365-246X.1981.tb04892.x>
- Meunier, J., Sultan, N., Jegou, P., & Harmegnies, F. (2004). First tests of Penfeld: A new seabed penetrometer. Paper presented at the Fourteenth International Offshore and Polar Engineering Conference.

- Migeon, S., Cattaneo, A., Hassoun, V., Dano, A., Casadevant, A., & Ruellan, E. (2012). Failure processes and gravity-flow transformation revealed by high-resolution AUV swath bathymetry on the Nice continental slope (Ligurian Sea). In *Submarine mass movements and their consequences* (pp. 451–461). Springer. https://doi.org/10.1007/978-94-007-2162-3_40
- Mogollón, J. M., Dale, A. W., L'Heureux, I., & Regnier, P. (2011). Impact of seasonal temperature and pressure changes on methane gas production, dissolution, and transport in unfractured sediments. *Journal of Geophysical Research*, *116*(G3). <https://doi.org/10.1029/2010JG001592>
- Morgan, E. C., Vanneste, M., Lecomte, I., Baise, L. G., Longva, O., & McAdoo, B. (2012). Estimation of free gas saturation from seismic reflection surveys by the genetic algorithm inversion of a P-wave attenuation model. *Geophysics*, *77*(4), R175–R187. <https://doi.org/10.1190/geo2011-0291.1>
- Nageswaran, S. (1983). *Effect of gas bubbles on the seabed behaviour* (D.Phil. Thesis). Oxford University.
- Oehler, T., Mogollón, J. M., Moosdorf, N., Winkler, A., Kopf, A., & Pichler, T. (2017). Submarine groundwater discharge within a landslide scar at the French Mediterranean coast. *Estuarine, Coastal and Shelf Science*, *198*, 128–137. <https://doi.org/10.1016/j.ecss.2017.09.006>
- Rocco, S., Woods, A. W., Harrington, J., & Norris, S. (2017). An experimental model of episodic gas release through fracture of fluid confined within a pressurized elastic reservoir. *Geophysical Research Letters*, *44*(2), 751–759. <https://doi.org/10.1002/2016gl071546>
- Roesner, A., Wiemer, G., Kreiter, S., Wenau, S., Wu, T.-W., Courbouloux, F., et al. (2019). Impact of seismicity on Nice slope stability—Ligurian Basin, SE France: A geotechnical revisit. *Landslides*, *16*(1), 23–35. <https://doi.org/10.1007/s10346-018-1060-7>
- Ruffine, L., Caprais, J.-C., Bayon, G., Riboulot, V., Donval, J.-P., Etoubleau, J., et al. (2013). Investigation on the geochemical dynamics of a hydrate-bearing pockmark in the Niger Delta. *Marine and Petroleum Geology*, *43*, 297–309. <https://doi.org/10.1016/j.marpetgeo.2013.01.008>
- Schmidt, F., Koch, B. P., Goldhammer, T., Elvert, M., Witt, M., Lin, Y.-S., et al. (2017). Unraveling signatures of biogeochemical processes and the depositional setting in the molecular composition of pore-water DOM across different marine environments. *Geochimica et Cosmochimica Acta*, *207*, 57–80. <https://doi.org/10.1016/j.gca.2017.03.005>
- Seeberg-Elverfeldt, J., Schlüter, M., Feseker, T., & Kölling, M. (2005). Rhizon sampling of porewaters near the sediment-water interface of aquatic systems. *Limnology and Oceanography: Methods*, *3*(8), 361–371. <https://doi.org/10.4319/lom.2005.3.361>
- SHOM. (2005). NRC2005-009 Norme du SHOM sur la mesure des hauteurs d'eau.
- Sills, G. C., & Thomas, S. D. (2002). Pore pressures in soils containing gas. In *Chemo-mechanical coupling in clays: From nano-scale to engineering applications* (pp. 211–222). Routledge.
- Sills, G. C., & Wheeler, S. J. (1992). The significance of gas for offshore operations. *Continental Shelf Research*, *12*(10), 1239–1250. [https://doi.org/10.1016/0278-4343\(92\)90083-V](https://doi.org/10.1016/0278-4343(92)90083-V)
- Sills, G. C., Wheeler, S. J., Thomas, S. D., & Gardner, T. N. (1991). Behaviour of offshore soils containing gas bubbles. *Géotechnique*, *41*(2), 227–241. <https://doi.org/10.1680/geot.1991.41.2.227>
- Sobkowitz, J. C., & Morgenstern, N. R. (1984). The undrained equilibrium behaviour of gassy sediments. *Canadian Geotechnical Journal*, *21*(3), 439–448. <https://doi.org/10.1139/t84-048>
- Stegmann, S., Sultan, N., Kopf, A., Apprioual, R., & Pelleau, P. (2011). Hydrogeology and its effect on slope stability along the coastal aquifer of Nice, France. *Marine Geology*, *280*(1–4), 168–181. <https://doi.org/10.1016/j.margeo.2010.12.009>
- Steiner, A., Kopf, A. J., Henry, P., Stegmann, S., Apprioual, R., & Pelleau, P. (2015). Cone penetration testing to assess slope stability in the 1979 Nice landslide area (Ligurian Margin, SE France). *Marine Geology*, *369*, 162–181. <https://doi.org/10.1016/j.margeo.2015.08.008>
- Stigall, J., & Dugan, B. (2010). Overpressure and earthquake initiated slope failure in the Ursa region, northern Gulf of Mexico. *Journal of Geophysical Research: Solid Earth*, *115*(B4). <https://doi.org/10.1029/2009jb006848>
- Stranne, C., O'Regan, M., Dickens, G. R., Crill, P., Miller, C., Preto, P., & Jakobsson, M. (2016). Dynamic simulations of potential methane release from East Siberian continental slope sediments. *Geochemistry, Geophysics, Geosystems*, *17*(3), 872–886. <https://doi.org/10.1002/2015gc006119>
- Sultan, N., Garziglia, S., Bompais, X., Woerther, P., Witt, C., Kopf, A., & Migeon, S. (2020). Transient groundwater flow through a coastal confined aquifer and its impact on nearshore submarine slope instability. *Journal of Geophysical Research: Earth Surface*, *125*(9), e2020JF005654. <https://doi.org/10.1029/2020JF005654>
- Sultan, N., Marsset, B., Ker, S., Marsset, T., Voisset, M., Vernant, A.-M., et al. (2010). Hydrate dissolution as a potential mechanism for pockmark formation in the Niger delta. *Journal of Geophysical Research: Solid Earth*, *115*(B8). <https://doi.org/10.1029/2010jb007453>
- Sultan, N., Savoye, B., Jouet, G., Leynaud, D., Cochonat, P., Henry, P., et al. (2010). Investigation of a possible submarine landslide at the Var delta front (Nice continental slope, southeast France). *Canadian Geotechnical Journal*, *47*(4), 486–496. <https://doi.org/10.1139/t09-105>
- Sultan, N., Voisset, M., Marsset, T., Vernant, A. M., Cauquil, E., Colliat, J. L., & Curinier, V. (2007). Detection of free gas and gas hydrate based on 3D seismic data and cone penetration testing: An example from the Nigerian Continental Slope. *Marine Geology*, *240*(1), 235–255. <https://doi.org/10.1016/j.margeo.2007.02.012>
- Terzariol, M., Sultan, N., Apprioual, R., & Garziglia, S. (2021). Pore habit of gas in gassy sediments. *Journal of Geophysical Research: Solid Earth*, *126*(5), e2020JB021511. <https://doi.org/10.1029/2020JB021511>
- Thomas, S. D., & Sills, G. C. (1990). Wave generated pore pressures in the seabed. In *Soil Mechanics Report NSM104/90*. University of Oxford.
- Tjelta, T. I., Svano, G., Strout, J. M., Forsberg, C. F., Johansen, H., & Plank, S. (2007). Shallow gas and its multiple impact on a North Sea production platform. Offshore site investigation and geotechnics: Confronting new challenges and sharing knowledge. Retrieved from <https://www.onepetro.org/conference-paper/SUT-OSIG-07-205>
- Tørum, A. (2007). Wave-induced pore pressures—Air/Gas content. *Journal of Waterway, Port, Coastal, and Ocean Engineering*, *133*(1), 83–86. [https://doi.org/10.1061/\(ASCE\)0733-950X](https://doi.org/10.1061/(ASCE)0733-950X)
- Tóth, Z., Spiess, V., Mogollón, J. M., & Jensen, J. B. (2014). Estimating the free gas content in Baltic Sea sediments using compressional wave velocity from marine seismic data. *Journal of Geophysical Research: Solid Earth*, *119*(12), 8577–8593. <https://doi.org/10.1002/2014JB010989>
- Turekian, K. K., Steele, J. H., & Thorpe, S. A. (2010). *A derivative of the encyclopedia of ocean sciences: Marine chemistry & geochemistry*. Elsevier.
- Vanneste, M., Sultan, N., Garziglia, S., Forsberg, C. F., & L'Heureux, J.-S. (2014). Seafloor instabilities and sediment deformation processes: The need for integrated, multi-disciplinary investigations. *Marine Geology*, *352*, 183–214. <https://doi.org/10.1016/j.margeo.2014.01.005>
- Vardy, M. E., Vanneste, M., Henstock, T. J., Clare, M. A., Forsberg, C. F., & Provenzano, G. (2017). State-of-the-art remote characterization of shallow marine sediments: The road to a fully integrated solution. *Near Surface Geophysics*, *15*(4), 387–402. <https://doi.org/10.3997/1873-0604.2017024>

- Wang, K., Davis, E. E., & van der Kamp, G. (1998). Theory for the effects of free gas in subsea formations on tidal pore pressure variations and seafloor displacements. *Journal of Geophysical Research: Solid Earth*, *103*(B6), 12339–12353. <https://doi.org/10.1029/98JB00952>
- Wilkins, R. H., & Richardson, M. D. (1998). The influence of gas bubbles on sediment acoustic properties: In situ, laboratory, and theoretical results from Eckernförde Bay, Baltic sea. *Continental Shelf Research*, *18*(14), 1859–1892. [https://doi.org/10.1016/S0278-4343\(98\)00061-2](https://doi.org/10.1016/S0278-4343(98)00061-2)
- Yamamoto, S., Alcauskas, J. B., & Crozier, T. E. (1976). Solubility of methane in distilled water and seawater. *Journal of Chemical and Engineering Data*, *21*(1), 78–80. <https://doi.org/10.1021/jc60068a029>
- Zillmer, M. (2006). A method for determining gas-hydrate or free-gas saturation of porous media from seismic measurements. *Geophysics*, *71*(3), N21–N32. <https://doi.org/10.1190/1.2192910>